TAMPEREEN TEKNILLINEN YLIOPISTO
TAMPERE UNIVERSITY OF TECHNOLOGY

JUSSI SYVÄOJA

A MULTIRESOLUTION APPROACH TO THE WAVEFORM TOMOGRAPHY INVERSE PROBLEM

Master of Science thesis

Tarkastaja: Sampsa Pursiainen ja Jari Hyttinen
Tarkastaja ja aihe hyväksytty
Luonnontieteiden tiedekunnan
tiedekuntaneuvoston
kokouksessa 9.3.2016

ABSTRACT

JUSSI SYVÄOJA: A multiresolution approach to the waveform tomography inverse problem
Tampere University of Technology
Master of Science thesis, 56 pages, 0 Appendix pages
May 2016
Master's Degree Programme in Science and Engineering
Major: Mathematics
Examiner: Sampsa Pursiainen ja Jari Hyttinen
Keywords: Full waverfom inversion, inversion problem, full waveform tomography, tomography, multiresolution

Full waveform tomography refers to a technique that can used in imaging internal structures of a target object without altering or damaging it in anyway. The term full waveform means that the wave is utilized in its full form. The imaging can be done using either acoustic waves or electromagnetic waves.

The goal of this thesis is to explore the concept of waveform inversion, the physical theory behind it and possible applications in real life. In the computational part of this thesis a multiresolution approach to solve a mathematical waveform inversion problem is introduced. The numerical test setup was based on a minimal configuration of three sources. A single resolution approach was used as a reference method. Numerical experiments were conducted in a 2D domain and the results of the multi- and single resolution were compared to each other.

Based on the results of the numerical experiments the multiresolution approach turned out to be a feasible method to solve our inversion problem. In addition to the memory savings gained compared to the single resolution method, the multiresolution also proved to be more accurate with suitably chosen regularization parameters.

TIIVISTELMÄ

JUSSI SYVÄOJA: Multiresoluutio lähestymistapana aaltomuodon tomografian inversio-ongelmaan
Tampereen teknillinen yliopisto
Diplomityö, 56 sivua, 0 liitesivua
toukokuu 2016
Teknisluonnontieteellinen koulutusohjelma
Pääaine: Matematiikka
Tarkastajat: Sampsa Pursiainen ja Jari Hyttinen
Avainsanat: Täyden aaltomuodon inversio, inversio-ongelma, täyden aaltomuodon tomografia, tomografia, multiresoluutio

Täyden aaltomuodon tomografia viittaa tekniikkaan, jota voidaan käyttää kohdekappaleen sisäisien rakenteiden kuvantamiseen vahingoittamatta sitä millään tavalla. Terminä täysi aaltomuoto tarkoittaa, että aalto hyödynnetään kokonaisuudessaan. Kuvantaminen voidaan tehdä tehdä käyttäen joko akustisia tai elektromageneettisia aaltoja.

Tämän diplomityön tarkoituksena on tutustua aaltomuotoisen inversion käsitteeseen, taustalla olevaan fysikaaliseen teoriaan sekä mahdollisiin käytännön sovelluksiin. Työn laskennallisessa osuudessa esitellään multiresoluutio ratkaisutapana matemaattiseen aaltomuotoiseen inversio-ongelmaan. Numeerinen testausjärjestely perustui kolmen lähteen muodostamaan minimaaliseen konfiguraatioon. Single-resoluutio lähestymistapaa käytettiin vertailumetodina. Numeeriset kokeet suoritettiin kaksiulotteisessa alueessa ja näitä kahta lähestymistapaa käyttäen saatuja tuloksia vertailtiin keskenään.

Saatujen tuloksien perusteella multiresoluutio osoittautui toteuttamiskelpoiseksi tavaksi ratkaista kyseinen inversio-ongelma. Laskennassa saavutettujen muistisäästöjen lisäksi multiresoluutio osoittautui myös single-resoluutiota täsmällisemmäksi tekniikaksi käytettäessä sopivasti valittuja regularisointiparametreja.

CONTENTS

1. Introduction 1

2. Background 3

2.1 Physical Basis 3

2.1.1 Maxwell's equations 3

2.1.2 Electromagnetic Wave Equation 6

2.1.3 Acoustic Wave Equation 10

2.2 Applications 11

2.2.1 Ultrasonic pulse velocity test on concrete 12

2.2.2 Ultrasound computer tomography in breast cancer detection . . . 13

2.2.3 Microwave tomography (MWT) in extremities soft-tissue imaging 15

2.2.4 Ground penetrating radar (GPR) 16

2.2.5 Ocean acoustic tomography 19

3. Mathematics 22

3.1 Forward model 22

3.2 Forward simulation 24

3.2.1 Differentiated signal 27

3.2.2 Signal reciprocity and deconvolution 29

3.3 Multiresolution computation 31

3.4 Inverse problem 32

3.4.1 Single resolution inversion 32

3.4.2 Multiresolution inversion 33

4. Numerical Experiments 35

4.1 Permittivity 35

4.2 Conductivity 35

4.3 Signal 35

4.4 Noise 36

4.5 Forward computations 37

4.6 Regularization 37
4.7 Accuracy 37
4.7.1 Error of relative overlap 37
4.7.2 Error of the value 38
4.7.3 Total variation 38
4.8 Robustness 38
5. Results 39
5.1 Error of relative overlap 39
5.2 Error of value 40
5.3 Total variation 44
5.4 Robustness analysis 44
5.5 Reconstructions 45
6. Discussion 48
7. Conclusions 51
Bibliography 52

LIST OF FIGURES

2.1 UPV testing of concrete 13

2.2 Examination table for 3D USCT 14

2.3 Simulated image of pig thigh 16

2.4 Ground Penetrating Radar (GPR) 17

2.5 Speed of sound in Ocean Acoustic Tomography 20

3.1 Picture of nodal function 24

3.2 Picture of element indicator function 25

3.3 Reciprocity and deconvolution 31

3.4 Formation of the denser mesh with multiresolution 32

3.5 Three triangular finite element meshes with different resolutions . . . 32

4.1 Configurations 36

5.1 Error of the relative overlap and error of the value with dense configuration 41

5.2 Error of the relative overlap and error of the value with normal configuration 42

5.3 Error of the relative overlap and error of the value with sparse configuration 43

5.4 Total variations 44

5.5 Robustness analysis 45

5.6 Picture of the construction to be recovered 46

5.7 Reconstructions and ROAs for configuration (A) 46

5.8 Reconstructions and ROAs for configuration (B) 47

5.9 Reconstructions and ROAs for configuration (C) 47

LIST OF TABLES

4.1 Specifications of the signal configurations (A) - (C) 36

LIST OF ABBREVIATIONS AND SYMBOLS

FDTD	Finite difference time domain
FEM	Finite element method
GPR	Ground Penetrating Radar
MWT	Microwave tomography

$\mathbf{E}$	electric field intensity
$\nabla \cdot \mathbf{E}$	divergence of electric field
$\nabla \times \mathbf{E}$	curl of electric field intensity
$\mathbf{B}$	magnetic flux density
$\nabla \cdot \mathbf{B}$	divergence of magnetic flux density
$\nabla \times \mathbf{B}$	curl of magnetic flux density
ρ	electric charge
t	time
$\frac{\partial \mathbf{B}}{\partial t}$	time derivative of magnetic flux density $\mathbf{B}$
μ	permeability
ε	permittivity
$\mathbf{J}$	electric current
$\frac{\partial \mathbf{E}}{\partial t}$	time derivative of electric field density $\mathbf{E}$
$\mathbf{D}$	electric flux density
$\nabla \cdot \mathbf{D}$	divergence of electric flux density
$\mathbf{H}$	magnetic field intensity
$\nabla \times \mathbf{H}$	curl of magnetic field intensity
$\frac{\partial \mathbf{D}}{\partial t}$	time derivative of electric flux density $\mathbf{D}$
μ_0	permeability of vacuum
ε_0	permittivity of vacuum
χ	electric susceptibility
χ_m	magnetic susceptibility
$\mathbf{P}$	dielectric polarization
$\mathbf{M}$	magnetization
σ	conductivity
c	speed of light
ϕ	electric vector potential
$\mathbf{A}$	electric scalar potential
$\nabla \times \mathbf{A}$	curl of electric scalar potential
$\nabla\phi$	gradient of electric vector potential
$[0, T]$	time interval

Ω	spatial domain
$\frac{\partial f}{\partial t}$	time derivative of signal f
$\frac{\partial^2 f}{\partial t^2}$	second order partial derivative of f with respect to t
Δ	Laplace operator
$\vec{x}$	vector x
∇u	Gradient of u
$\nabla \cdot \vec{g}$	divergence of $\vec{g}$
$\int_\Omega$	Integral over the domain Ω
$\mathbf{A}$	Matrix A
$\mathbf{p}$	vector p

1. INTRODUCTION

The term tomography refers to group of non-invasive methods that are used to form image of the internal structures of a target object. In general, tomographic imaging can be performed using any kind of penetrating wave [1] [2]. In full waveform tomographic imaging the wave is inverted in its full form. This type of imaging could be done using either sound waves on ultrasonic and acoustic frequencies or electromagnetic waves on microwave and radiowave frequencies.

The introduction of the theory behind full waveform tomography goes back several decades. However, until recently it has not been employed even close to its full potential in the scientific world. The reason to this has mostly been the complexity and non-linearity of the calculations regarding the inversion procedure. Both the computer's ability to compute and the limited number of people that understand these kind of calculations have restricted the development of full waveform tomographic applications [3]. Nevertheless, full waveform tomography is already widely utilized in several fields of science from geophysics to medical science. One target of this thesis is to consider these possible applications of full waveform tomography and some examples of these applications are introduced further in this work.

The mathematical model in this thesis is only applied in 2D domain but most of the practical real life applications require the use of 3D model to achieve desired results. For example, in the biomedical ultrasonic and microwave imaging it is significantly beneficial if the image of the targeted tissue could be constructed three-dimensionally [4], [5] [6], [7], [8]. In the case of ultrasonic testing of concrete the 3D model could also be beneficial but the use of the 2D model could be sufficient in measurement of the transit time of the signal through concrete [9] [10]. In geological inspections the ground penetrating radar can be utilized either two- or three-dimensionally [11]. With the ocean acoustic tomography the model is only two-dimensional as the measurements are based on the changes in the temperature of the seawater that alter the travel time of a signal [12], [13].

In the mathematical part of this thesis, both a multiresolution and single resolution approaches to solve a waveform inversion problem are introduced. The mathetical

model that is used in this thesis is based on three sources that transmit certain signals and on the signal receivers that record these signals in the measuring points. Also the backscattering of the signal was implemented in that model. Based on the data gathered by these receivers the goal is to reconstruct the internal permittivity distribution of the targeted objects. The crucial concepts regarding this kind of forward model are the finite-difference time-domain (FDTD) method and the deconvolution process which enabled computation of both the actual and the differentiated signal. Also the reciprocity of the signal was utilised [14]. The finite element method (FEM) is applied to achieve the spatial discretization of the computational domain [15]. The leapfrog time integration method is used to simulate the signal in that discretized domain. The inversion prodecure that is used to recover the permittivity of the target objects is total variation regularized and implemented in the finite element mesh.

The numerical experiments were performed in a 2D-domain using both the single and the multiresolution approaches. The test domain consisted of three vacuum cavities together with a surface layer. Three different kinds of signal configurations, dense, medium and sparse were used. Calculations were also executed for the variety of different values of regularization parameters. The results of these numerical experiments show that the multiresolution approach is fully applicable and even works better than the reference single resolution approach when choosing the parameters appropriately.

2. BACKGROUND

This chapter gives basic background infromation behind full waveform tomography. First we are going explore the electromagneticl basis by introducing the Maxwell's equations and explaining how one could obtain electromagnetic wave function out of them. It is also shown that a similar wave equation applies for the acoustic waves as well. Then, we consider possible applications of full waveform tomography in different areas of science and give a short introduction on each of those applications.

2.1 Physical Basis

2.1.1 Maxwell's equations

Maxwell's equations are a set of four fundamental relations that any electromagnetic field should satisfy under time-varying conditions. They form the unified theory of electricity and magnetism. These equations always hold regardless of the material medium. The name Maxwell's equations refers to James Clerk Maxwell who was a physicist and a mathematician that first wrote down these equations in complete form in 1873 by formulating previously known experimental results of Coulomb, Gauss, Ampére, Faraday and others, and by adding the displacement current term to the last equation. The equations could be written in two different forms that are the microscopic and the macroscopic equations [16].

Microscopic equations

Maxwell's equations in the microscopic form use total charge and total current. These equations include also the complicated atomic level currents and charges in materials. The equations in this form have universal applicability but it may be impossible to do the calculations in practice. Microscopic equations are also known as the general form of Maxwell's equations or the Maxwell's equations in a vacuum. The use of word vacuum here does not mean the absence of any charges or currents in the space used but it refers to the fact that the material medium is not built in structure of the equation [16]. The microscopic form of the equations can be expressed as follows:

$$\text{Gauss's Law} \qquad \nabla \cdot \mathbf{E} = \frac{\rho}{\varepsilon} \tag{2.1}$$

$$\text{Gauss's Law for magnetism} \qquad \nabla \cdot \mathbf{B} = 0 \tag{2.2}$$

$$\text{Maxwell-Faraday equation} \qquad \nabla \times \mathbf{E} = -\frac{\partial \mathbf{B}}{\partial t} \tag{2.3}$$

$$\text{Ampére's circuital law} \qquad \nabla \times \mathbf{B} = \mu \left(\mathbf{J} + \varepsilon \frac{\partial \mathbf{E}}{\partial t} \right) \tag{2.4}$$

The quantities **E** and **B** in these equations are the electric field intensity and magnetic flux density. The field **B** is sometimes also called magnetic induction. The universal constants ε and μ are the permittivity and the permeability of the material. Permittivity is a measure that describes how a material resists an electric field that affects to it. Permeability in turn measures the ability of material to support the formation of a magnetic field within itself [17].

Macroscopic equations

Macroscopic Maxwell's equations, sometimes also referred as Maxwell's equations in matter are more similar to the form that Maxwell himself first introduced. The macroscopic form does not consider the atomic scale details as in the microscopic case, but instead defines two new auxiliary fields that describe the behavior in larger scale. The use of macrosopic equations requires the introduction of constant relations that describe the electromagnetic properties of the concerning substances [16]. The equations in the macroscopic form are

$$\text{Gauss's Law} \qquad \nabla \cdot \mathbf{D} = \rho \tag{2.5}$$

$$\text{Gauss's Law for magnetism} \qquad \nabla \cdot \mathbf{B} = 0 \tag{2.6}$$

$$\text{Maxwell-Faraday equation} \qquad \nabla \times \mathbf{E} = -\frac{\partial \mathbf{B}}{\partial t} \tag{2.7}$$

$$\text{Ampère's circuital law} \qquad \nabla \times \mathbf{H} = \mathbf{J} + \frac{\partial \mathbf{D}}{\partial t}. \tag{2.8}$$

In addition to microscopic equations there are now two new fields **H** and **D** that are magnetic field intensity and electric flux density. The field **D** is sometimes also called the electric displacement [17].

Constitutive equations

In electromagnetism, electric and magnetic flux densities are always related to electric and magnetic field intensities **E** and **H**. The specification of these relations is necessary in order to utilize the macroscopic form of Maxwell's equations and to do calculations using them. The equations that specify these relations are called constitutive equations. The form of these equations depends on the material in which the electromagnetic field exists [17]. In a vacuum they take their simplest form

$$\mathbf{D} = \varepsilon_0 \mathbf{E} \tag{2.9}$$

$$\mathbf{H} = \frac{1}{\mu_0}\mathbf{B} \tag{2.10}$$

where ε_0 and μ_0 that are the permittivity and the permeability of vacuum. For magnetic and simple homogenous isotropic dielectric materials the equations are:

$$\mathbf{D} = \varepsilon \mathbf{E} \tag{2.11}$$

$$\mathbf{H} = \frac{1}{\mu}\mathbf{B} \tag{2.12}$$

These equations are typically valid at low frequencies. The permittivity of the material ε and permeability of the material μ are always related to the electric and magnetic susceptibilities of the material. These relations are:

$$\varepsilon = \varepsilon_0(1+\chi) \tag{2.13}$$

$$\mu = \mu_0(1+\chi_m). \tag{2.14}$$

The susceptibilities χ, χ_m describe the electric and the magnetic polarization characteristics of the material. For the electric flux density we have

$$\mathbf{D} = \varepsilon\mathbf{E} = \varepsilon_0(1+\chi)\mathbf{E} = \varepsilon_0\mathbf{E} + \varepsilon_0\chi\mathbf{E} = \varepsilon_0\mathbf{E} + \mathbf{P}, \tag{2.15}$$

where $\mathbf{P} = \varepsilon_0\chi\mathbf{E}$ stand for the dielectric polarization of the material. It is defined

as the average electric dipole moment per unit volume. For a magnetic material we have:

$$\mathbf{B} = \mu_0(\mathbf{H} + \mathbf{M}) = \mu_0(\mathbf{H} + \chi_m\mathbf{H}) = \mu_0(1 + \chi_m)\mathbf{H} = \mu\mathbf{H}, \tag{2.16}$$

where $\mathbf{M} = \chi_m\mathbf{H}$ represents the magnetization, which is defined as the average magnetic moment per unit volume [17].

The definitions of the Maxwell's equations

Gauss's law describes the relationship between a static electric field and the electric charges that cause it. The law states that the net outward electric flux passing through any closed surface is equal to the total charge enclosed by that surface. [16]

Gauss's law for magnetism, sometimes known also as "Absence of free magnetic poles" states that the divergence of a magnetic field $\mathbf{B}$ is equal to zero. In other words this means that the net outward magnetic flux through a closed surface is always zero. [16]

The Maxwell-Faraday equation also known as Faraday's law of induction describes how a time varying magnetic field creates (induces) an electric field. It states that the induced electromotive force in a wire loop is equal to the negative time rate of change of the magnetic flux linkage with the loop. [16]

Ampere's circuital law also known as the Maxwell-Ampère equation relates the integrated magnetic field around a closed loop to the electric current passing through the loop. It states that the line integral of magnetic field around a closed path is equal to the total current enclosed by that path. [16]

2.1.2 Electromagnetic Wave Equation

The electromagnetic wave equation, as the basic wave equation, is a linear second-order partial differential equation. It is an important equation for the description of how electromagnetic waves propagate through a medium or in a vacuum. It is a three-dimensional form of the wave equation and works as a solution to the Maxwell's equations [16]. It is explained in this section how one can obtain electromagnetic wave equation from the maxwell's equations first for dielectric materials and then for conductive materials. In the end it is shown that the wave equation could also be written for potential fields.

Wave Equation in dielectric media

The material here is considered to be 'simple' meaning that it is linear (μ and ε are constants), isotropic, homogenous, source-free ($\rho = 0$) and non-conducting ($\mathbf{J}= 0$). Maxwell's equations then reduce in this case to the following form

$$\nabla \cdot \mathbf{E} = 0 \tag{2.17}$$

$$\nabla \cdot \mathbf{B} = 0 \tag{2.18}$$

$$\nabla \times \mathbf{E} = -\frac{\partial \mathbf{B}}{\partial t} \tag{2.19}$$

$$\nabla \times \mathbf{B} = \mu_0 \varepsilon_0 \frac{\partial \mathbf{E}}{\partial t}. \tag{2.20}$$

First taking the curl of the curl equations (2.19), (2.20) gives

$$\nabla \times (\nabla \times \mathbf{E}) = -\frac{\partial}{\partial t} \nabla \times \mathbf{B} = -\mu_0 \varepsilon_0 \frac{\partial^2 \mathbf{E}}{\partial t^2} \tag{2.21}$$

$$\nabla \times (\nabla \times \mathbf{B}) = -\mu_0 \varepsilon_0 \frac{\partial}{\partial t} \nabla \times \mathbf{E} = -\mu_0 \varepsilon_0 \frac{\partial^2 \mathbf{B}}{\partial t^2} \tag{2.22}$$

Now using the vector identity $\nabla \times (\nabla \times \mathbf{V}) = \nabla(\nabla \cdot \mathbf{V}) - \nabla^2 \mathbf{V}$ and equations (2.17) and (2.17) that state $\nabla \cdot \mathbf{E} = 0$ and $\nabla \cdot \mathbf{B} = 0$ we can obtain the wave equations

$$\nabla^2 \mathbf{E} = \mu_0 \varepsilon_0 \frac{\partial^2 \mathbf{E}}{\partial t^2} \tag{2.23}$$

$$\nabla^2 \mathbf{B} = \mu_0 \varepsilon_0 \frac{\partial^2 \mathbf{B}}{\partial t^2} \tag{2.24}$$

The first one is a homogenous wave equation for the electric field and the second one a homogenous wave equation for the magnetic field. This kind of wave propagates at a speed $c_0 = 1/\sqrt{\varepsilon_0 \mu_0}$ which is the speed of light in vacuum [18] [19].

Wave equation in conductive media

In conductive media there applies a constitutive relation $\mathbf{J} = \sigma \mathbf{E}$, where σ is a

constant, the conductivity of the material. It is also assumed that there are free charges ρ present. Maxwell's equations now take the form

$$\begin{aligned} \nabla \cdot \mathbf{E} &= \frac{\rho}{\varepsilon} && (2.25)\\ \nabla \cdot \mathbf{B} &= 0 && (2.26)\\ \nabla \times \mathbf{E} &= -\frac{\partial \mathbf{B}}{\partial t} && (2.27)\\ \nabla \times \mathbf{B} &= \mu\left(\sigma\mathbf{E} + \varepsilon\frac{\partial \mathbf{E}}{\partial t}\right). && (2.28) \end{aligned}$$

Let us first consider the wave equation for the electric field. Taking the curl of the equation (2.27) and placing the right hand side of the equation (2.28) in it gives

$$\nabla \times (\nabla \times \mathbf{E}) = -\frac{\partial}{\partial t}\nabla \times \mathbf{B} = -\mu\sigma\frac{\partial \mathbf{E}}{\partial t} - \mu\varepsilon\frac{\partial^2 \mathbf{E}}{\partial t^2}. \tag{2.29}$$

Then using the same vector identity as before and the equation (2.25) we get

$$\nabla^2\mathbf{E} - \mu\varepsilon\frac{\partial^2 \mathbf{E}}{\partial t^2} - \mu\sigma\frac{\partial \mathbf{E}}{\partial t} = \frac{1}{\varepsilon}\nabla\rho \tag{2.30}$$

For the magnetic field the steps are pretty similar. First taking the curl of the equation (2.28) and applying equation (2.27) yields

$$\nabla \times (\nabla \times \mathbf{B}) = \mu\sigma\nabla \times \mathbf{E} + \mu\varepsilon\frac{\partial}{\partial t}\nabla \times \mathbf{E} = -\mu\sigma\frac{\partial \mathbf{B}}{\partial t} - \mu\varepsilon\frac{\partial^2 \mathbf{B}}{\partial t^2}. \tag{2.31}$$

Then applying the vector identity and using equation (2.26) we get

$$\nabla^2\mathbf{B} - \mu\varepsilon\frac{\partial^2 \mathbf{B}}{\partial t^2} - \mu\sigma\frac{\partial \mathbf{B}}{\partial t} = 0. \tag{2.32}$$

The equation (2.30) is an electromagnetic wave equation for electric field in conductive material. It is of the inhomogenous form as there is a term $1/\varepsilon\nabla\rho$ on the right hand side of the equation caused by the presence of the free charges in the material. The equation (2.32) in turn is an electromagnetic wave equation for the magnetic field in a conductive material [20] [21].

Potential Fields

Potential fields also satisfy the electromagnetic wave equation. Let us now consider the Maxwell's equation in the case where there are not magnetic and polarizable material. First of all let us define the material here to be vacuumlike. Therefore the permittivitty and the permeability of the material are ε_0 and μ_0. The most efficient approach is to use the scalar and vector potentials ϕ and $\mathbf{A}$. It yields from the equation $\nabla \cdot \mathbf{B} = 0$ that the magnetic flux density can be expressed in the form $\mathbf{B} = \nabla \times \mathbf{A}$. By placing this to Faraday's law we get

$$\nabla \times \mathbf{E} + \frac{\partial}{\partial t} \nabla \times \mathbf{A} = 0. \tag{2.33}$$

Then for physically smooth fields we can interchange the order of time and spatial derivatives and this yields to

$$\nabla \times \left(\mathbf{E} + \frac{\partial \mathbf{A}}{\partial t} \right) = 0 \tag{2.34}$$

so we can write $\mathbf{E} + \partial \mathbf{A}/\partial t = -\nabla \phi$. The electric field is therefore of the form

$$\mathbf{E} = -\nabla \phi - \frac{\partial \mathbf{A}}{\partial t} \tag{2.35}$$

in which the Faraday's law brings a new part to the electric field due to the time derivative of the vector potential $\mathbf{A}$. Now the Gauss's law and the The Ampère's circuital law can be expressed in the following form

$$\nabla^2 \phi + \frac{\partial (\nabla \cdot \mathbf{A})}{\partial t} = \frac{-\rho}{\varepsilon_0} \tag{2.36}$$

$$\nabla^2 \mathbf{A} - \frac{1}{c^2} \frac{\partial^2 \mathbf{A}}{\partial t^2} - \nabla \left(\nabla \cdot \mathbf{A} + \frac{1}{c^2} \frac{\partial \phi}{\partial t} \right) = -\mu_0 \mathbf{J}. \tag{2.37}$$

Then we can use the following Lorenz gauge condition in order to solve these equations

$$\nabla \cdot \mathbf{A} + \frac{1}{c^2} \frac{\partial \phi}{\partial t} = 0 \tag{2.38}$$

Finally, the remaining equations simplify into inhomogenous wave equations:

$$\left(\nabla^2 - \frac{1}{c^2}\frac{\partial^2}{\partial t^2}\right)\phi = \frac{-\rho}{\varepsilon_0} \tag{2.39}$$

$$\left(\nabla^2 - \frac{1}{c^2}\frac{\partial^2}{\partial t^2}\right)\mathbf{A} = -\mu_0\mathbf{J} \tag{2.40}$$

It is now proven that the electromagnetic wave equations can also be written for potential fields. The first equation is an inhomogenous wave equation for the vector potential as there is a source term on the right hand side due to presence of free charges ρ. The second equation is an inhomogenous wave equation for the scalar potential, where the source term comes from the presence of free currents $\mathbf{J}$ [20].

2.1.3 Acoustic Wave Equation

A very similar equation that was introduced before for electromagnetic waves can be written for acoustic waves as well. In fact, this equation played a big part in the development of the electromagnetic wave equation and is called the acoustic wave equation. It describes the propagation of acoustic waves through a material medium. It should be noted here that the acoustic wave equation does not have the applicability in a vacuum as the acoustic waves could only propagate in a material medium. A most simple form of this equation that applies for the acoustic waves in only one dimension can be written as [22] [23]:

$$\frac{\partial^2 p}{\partial x^2} - \frac{1}{c^2}\frac{\partial^2 p}{\partial t^2} = 0. \tag{2.41}$$

The equation in this form describes the evolution of acoustic pressure p as a function of position x and time t. The acoustic wave propagates on a speed of sound $c = \sqrt{B/\rho}$, where B is the bulk modulus that measures the substance's resistance to uniform compression and ρ is the density of the substance. The acoustic wave equation could also be written in more general form:

$$\nabla^2 p - \frac{1}{c^2}\frac{\partial^2 p}{\partial t^2} = 0. \tag{2.42}$$

The equation in this form describes the propagation of waves in three dimensions [23].

2.2 Applications

The concept of full waveform tomography, sometimes also full waveform inversion or just waveform inversion, has been known for decades but still did not make its breakthrough until recently. It has mainly been used only in academic institutes even though being a regular topic in academic world for a long time now. That is mostly because of the complexity of the calculations regarding the inversion. Another thing that has been restricting the use of full waveform tomography is the low computer power to compute such kind of calculations.

However, the years have passed and our ability to understand and manage this kind of complex and nonlinear inversions has developed. By the same time the calculation power of computers have risen explosively. [3] So it seems by now that there are no more that many reasons left to prevent the full waveform tomography from spreading more widely in the scientific world and becoming part of various applications on a daily basis. At least if not in the near future then during the following decades.

Even though the real potential of full waverform tomography has yet to be harnessed there are a few known applications already. One important application of waveform tomography is in the field of non-destructive testing (NDT), which is a group of analyzing methods used in science and industry in order to evaluate the characteristics of some test object. The analysis is performed without causing any damage to the test object or altering it in anyway [2]. In addition to a variety of other non-invasive techniques NDT testing can also be performed utilizing ultrasonic tomography. A very common test method that could be used in evaluating the properties of concrete is called ultrasonic pulse velocity test [9].

Another application of waveform tomography is in medical field, especially in breast cancer detection [4] [24]. The imaging in breast cancer detection is currently performed mostly using mammography, but alternative imaging methods have already been discussed and developed. That is mostly because of two things, the well-known risks of the X-radiation to the patient and the lack of sensitivity and specificity in mammography [5]. Ultrasound computer tomography (USCT) has turned out to be one of the most promising candidates and could be a very good alternative for mammography in the future [4].

Microwave tomography (MWT) could also be used in biomedical imaging of soft tissues as well as USCT. One clinical application of MWT is the imaging of soft tissues of extremities, but it is also applicable for breast cancer detection, diagnostics of lung cancer, brain imaging and cardiac imaging. The method is based on the high dielectric contrast between bones and fatty areas in comparison with soft tissues [6].

The fourth application relates to radiowave tomography and using radiowaves for examining the subsurface structures. A device called ground-penetrating radar (GPR) is an example of geophysical methods that use radio waves. It can be used in analyzing a variety of different types of subsurface objects [11].

The last application reviewed in this section is called Ocean Acoustic Tomography, a technique that uses acoustic waves in measuring of temperatures and currents in the oceans. The method relies on the conductivity of sound of seawater and the travel times of the sound signals in the ocean between two instruments [13].

2.2.1 Ultrasonic pulse velocity test on concrete

Ultrasonic pulse velocity test is normally performed using portable equipment, that consists of the source and the detector units and the surface transducers [9]. An example of the equipment in use is shown in figure 2.1. In an UPV test an ultrasonic pulse with a frequency of 25-60kHz is introduced into one surface of concrete by a transducer that is coupled to the surface with either coupling gel or grease. Then another similar transducer on the opposite surface of the concrete receives the pulse that traversed the concrete. The transit time of the pulse is monitored by the device and the pulse velocity could be calculated by dividing the distance between the transducers by the transit time [10]. The ultrasonic pulse depends on the elastic properties and the density of the concrete [9].

The UPV tests can be used to analyze various of properties of concrete. Normally it is performed in order to verify the uniformity of concrete, to detect internal imperfections, to evaluate the depth of these imperfections, to estimate the deformation moduli and the compressive strength or to monitor the characteristics variation of concrete through time.

Even slight changes in the concrete density, constitution and soundness affect the test as it is very sensitive. UPV could also be used to inspect the homogeneity of concrete and to find spots of which properties differ from the properties of the surrounding areas. In a case of composite materials it could also be used to measure the thickness of different layers.

The relation between the qualities of concrete with compressive strength could also be explored with UPV. This relies on the fact that ultrasonic waves depend on the density of the material and that they correlate with the compressive strength. However, as there are lot of variables that have an influence on the concrete strength, such as the water/cement ratio, the size of the sample and the cement type, the

Figure 2.1 *UPV testing of concrete using Pundit Plus, source: Germann Instruments*

relation is not always reliable.

UPV test could also be applied in some processes of concrete curing as it allows controlling of important parameters of concrete such as strength, elasticity module and shrinkage. The use of UPV methods in investigation of concrete structures is very advantageous as it enables the monitoring of the characteristics of the concrete through its service life. With ultrasonic data it is possible to define the concrete uniformity, to monitor its quality, to follow its deterioration and to estimate its strength by comparing control specimens [9].

2.2.2 Ultrasound computer tomography in breast cancer detection

Ultrasound computer tomography (USCT), ultrasound computed tomography or sometimes ultrasound computerized tomography [8] is a method that could be used in medical tomographic examinations. It utilizes ultrasound waves for creating images and is mostly used in imaging of soft tissue, especially in breast imaging [4]. The measurement could be divided into two steps. The ultrasound waves are transmitted in direction of the measurement object using piezoelectric transducers and received using either the same or other transducer. The travelling waves are changed by the measurement object when interacting with it and the waves then carry information

about the object that could be recorded. In the second step that information could be used to form an image of the object. In medical imaging, the USCT systems typically aim for a resolution of centimeters to millimeters and therefore the ultrasound waves used are approximately of 1 MHz frequency [8]. The examination table used for USCT is shown in 2.2.

Figure 2.2 *Examination table for 3D ultrasound computer tomography, source: Karlsruhe Intitute of Technology*

Using ultrasound computer tomography instead of traditional mammography can have several advantages. The first and probably the most important advantage of USCT in comparison with mammography is the use of ultrasound waves instead of X-rays. This makes breast imaging with USCT, which is a harmless and risk-free method, safer than with mammography as the problem has been the radiation caused by the X-rays that is known to be hazardous to the patient. Consequently, the dosage of radiation must have been monitored and strictly limited [5].

The weaknesses of mammography in terms of sensitivity and specificity are also well known [5]. This is where USCT could possibly make a big difference as it could provide multiple information of the object at the same time whereas mammography can only provide one information. This information produced by USCT contains recordings of speed-of-sound volume, attenuation and morphology among other things [**?**]. It is also very useful that the breast imaging using USCT can be performed without

the need of a physician as the positioning and image acquisition are standardized. A radiologist could diagnose the reconstructed images afterwards independently of the imaging process [4].

2.2.3 Microwave tomography (MWT) in extremities soft-tissue imaging

Understanding two major components of any segments of injured extremity is crucial in a succesful treatment of a fractured bone. These two components are the bony element and the soft-tissue element such as skin, muscle, nerve or vessels. The bony element is easily diagnosed and evaluated by the treating physician using radiographic studies, but the major deficiency in the treatment of fractures have been the lack of ability to accurately assess the soft-tissue component of the injured segments [6].

As microwave tomography (MWT) have proven to be successful in assessment of soft-tissue conditions it would provide, together with radiology, the treating surgeon a complete assessment of both components of any given injury. In the extremities there is a very high dielectric contrast between soft tissues and bones, but this is only useful in imaging the bones. One thing that additionally complicates the problem is that the dielectric contrast is much lower between soft-tissue abnormalities than it is between bone and soft-tissue. This problem, however, could be simplified as some segments of the extremity could be approximated two-dimensionally. This enables the use of a less complicated two-dimensional imaging approach instead of the more complicated three-dimensional imaging [6].

There have been a few experiments in order to access the applicability of MWT for extremities. These experiments have so far been conducted mostly on animals, but some test have also been conducted using volunteers. One example of the experiments conducted on animals is an experiment on a pig thigh with acute compartment syndrome and areas of reduced blood flow. A simulated microwave tomographic image of this experiment is presented in the figure 2.3. Based on the promising results of these experiments microwave tomography might be a mobile, safe and cost-effective alternative to current imaging modalities in the future for humans as well [6].

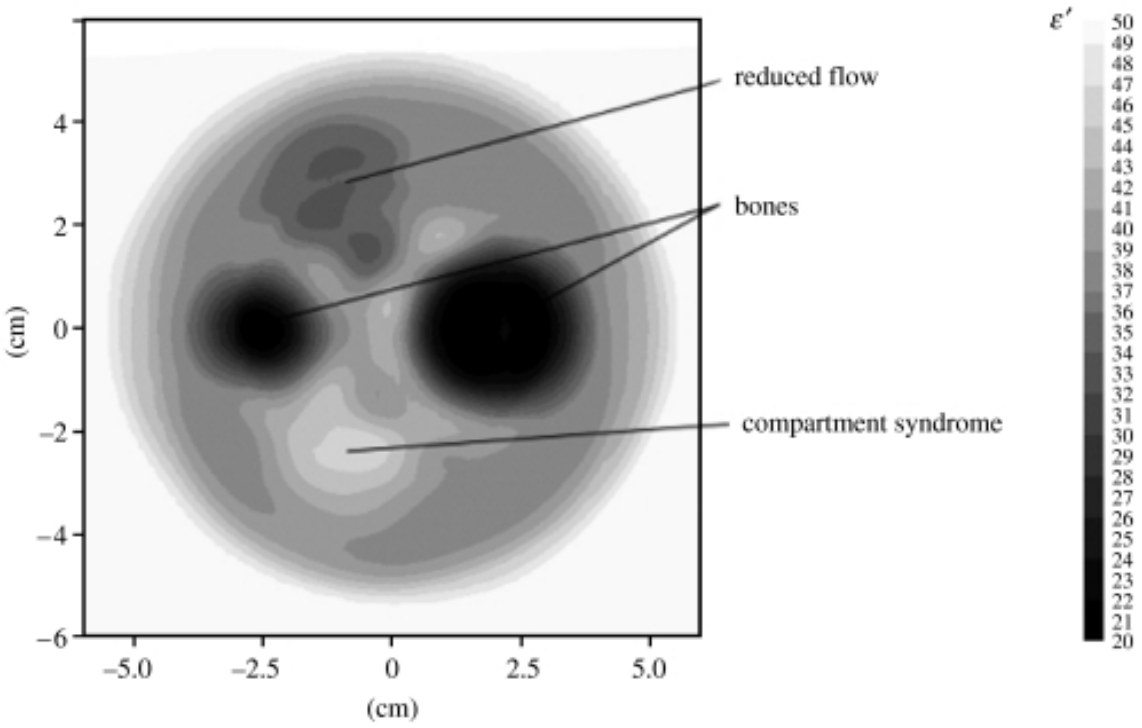

***Figure** 2.3 Simulated microwave tomographic image of pig thigh. The areas of compartment syndrome and reduced blood flow can clearly be seen in the picture, source: NCBI*

2.2.4 Ground penetrating radar (GPR)

Ground Penetrating Radar (GPR) is a device that uses radiowave radar pulses to form an image of subsurface. There are four requirements that are needed for GPR to operate succesfully: (1) the signal to clutter ratio, (2) the signal to noise ratio, (3) the spatial resolution of the target and (4) the depth resolution of the target need to be adequate. One type of GPR is presented in a figure 2.4.

The biggest strength of GPR is that it could be used in analyzing various of different types of subsurfaces and it could observe elements of different types and sizes. That is why GPR has applications in so many fields. A few of those applications are instructed below.

Archeology

In archeology, GPR has been used to locate voids, inconsistencies and buried metalwork in castles and Egyptian pyramids for example. To be able to use GPR properly in archeology, two types of professionals are needed. Those who have the knowledge of the actual capabilities of radar techniques such as radar or electrical engineers and those who have the knowledege of the construction systems such as architects or

Figure 2.4 *Radiodetection RD1000 Ground Penetrating Radar (GPR), source: Keison products*

structural engineers. GPR is best employed in archelogy when it is used alongside other applications such as magnometers, resistance and radio-detection devices [11].

Civil engineering

GPR has also some applications in civil engineering as it has become a routine method of inspection of civil engineering structures such as roads and pavements, concrete structures, bridges and tunnels.

In inspection of roads and pavements GPR can be used either hand propelled or alternatively mounted on a vehicle. These vehicle based systems can survey pavements with minimum distruption to the traffic economically, safely and speedily as typical vehicle based radar, at normal traffic speeds, can cover up to 300km a day. GPR is also a very effective technique for investigating the integrity of concrete structures. Enhanched inspection efforts are required today due to aging of concrete structures, but GPR can also be used as part of quality assurance systems in order to reduce high maintenance costs. Typical testing problems related to concrete structures are for example detection of reinforcement and tendon ducts, voids and honeycombing, and the detection of airgaps and moisture at interfaces.

Within buillt structures GPR can give information on presence, position or size of nonvisible features of buildings as well as on the quality of the known features. The bandwith of 0.3-1 GHz is the most suitable for the scale of objects in built structures [11].

Forensic investigation

GPR could also be used in forensic investigations as it could help in locating concealed and buried objects such as human remains, weapon caches, hides and drug caches. This could save a lot of time, money and manpower as GPR could pinpoint the suspicious areas. Therefore the inspected area could be narrowed down and the need of extensive and expensive excavation could be reduced [11].

Geophysics

In geophysics GPR have typically had applications such as probing of rocks, soils, snow and ice, but GPR could also be used in inspection of frozen materials. Since the invention of airborne systems the inpection of frozen materials these days is carried out mostly from helicopters and fixed wing aircrafts. These investigations locate primarily in the Antarctic.

In mining fields GPR have been used to investigate the boreholes. This kind of device is called a borehole radar. The parameter here is range as boreholes tend to be very deep. So the borehole radars typically use low frequencies; 20 and 60 MHz are the most common bandwidths. Borehole radar could also be used in short boreholes for geotechnical investigations. In this case resolution is emphasized so the radar uses frequencies that go as high as up to 1GHz [11].

Mine detection

In military use, GPR could help in detecting unexploded ordnance such as landmines. The main issue with GPR or any other mine detecting tehcniques is the probability of detection and false alarm rate. The most plausible mine detection device using GPR is the hand-held model that will be combined with a metal detector. Also vehicle mounted and airborne models have been developed and tested in practice. The vehicle mounted model can both look straight to the ground or look ahead in forward-look mode.

The main interest in developing more efficient mine detection techniques is the fact that the buried landmines have become a humanitarian challenge as they are very widely used over the world. The problem with landmines is that they cannot distinguish between a soldier and a civilian and they remain active for decades. This has lead to situation where most of the victims of the landmines have become civilians [11].

Utilities

GPR could also be used in detection of the utilies of plant. When commissioning organisations installate a new plant in place for an existing one their goal is to do the installation with minimum damage to the utilities of the existing plant including gas, water, sewage, electricity, telephone cable et cetera. This would enable the installation to be rapid and cost-effective.

There are still some constraints on the design of this kind of surface-penetrating radar system. While the majority of the buried plant is within 1.5 to 2 m of the ground surface, it may still have variation in its size. It may also be either metallic or nonmetallic and it may be in a close proximity to other plants. It may also buried in different soil types involving differences in electromagnetic absorption. If the ability to detect all buried plant down to 1.5m could be reached then approximately 90% of all buried plant could be located in all conditions. [11]

Remote sensing

GPR systems have also been used for remote sensing below the surface of the earth and the planets. These types of radar systems can be mounted either on aircrafts or satellites and they differ radically from other GPR systems that were introduced above. Most of the work in remote sensing is done utilizing a device called synthetic aperture radar (SAR). These SAR systems have been able to detect, for instance, buried metallic mines from a height of several hundred meters and a special SIR-C satellite SAR radar have imaged buried artefacts in desert conditions.

Imaging the subsurfaces with radars mounted on satellites or aircrafts is only possible where the topographic cover is radar smooth and the material is fine grained. The material also needs to be no more than few metres thick and very dry. The return signal have been detected to be significantly increased where the thickness of the cover is less than skin depth. That is mostly due to refraction of the electromagnetic wave and reduction of backscatter because of oblique incidence. The scale of the frequency of signal used in remote sensing is 0.1-1.5 GHz [11].

2.2.5 Ocean acoustic tomography

Ocean acoustic tomography is method that can be used in measuring the temperatures and ocean currents over wide areas of the ocean. This method is also known as acoustic thermometry on ocean basin scale. The technique is based on the use of a one acoustic receiver and a one acoustic source and the measuring of the time a sound signal takes to travel between these two devices. Typically several of this kind of source-receiver pairs are used in oceanographic experiments. The distance

between the source and the receiver is usually in the range of 100-5000km.

If the precise locations of these two devices are known, the speed of sound could be computed as an average over the acoustic path by utilizing the measurement of time-of-flight. The changes in the temperature of the ocean are the mean reason that cause the changes in the speed of sound. Therefore the measurement of the time-of-flight is equivalent to a measurement of temperature. A change of 1°C in the temperature leads approximately to a change of 4 m/s in the speed of sound [13]. Figure 2.5 expresses the distribution of the speed of sound in two experiments, AMODE and SYNOP.

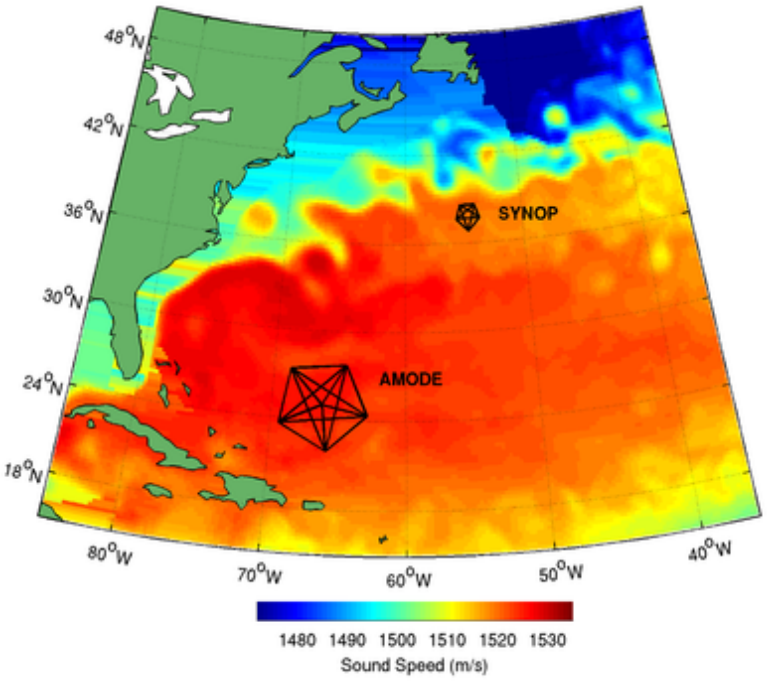

Figure 2.5 *A snapshot showing the changes in the speed of sound as a result of two experiments (AMODE and SONAP) that were performed in the western North Atlantic Ocean, source: Wikipedia*

The motivation behind the development of Ocean Acoustic Tomography was the electrical conductivity of seawater that makes the oceans opaque to electomagnetic energy. However, the oceans are fairly transparent to low-frequency acoustics as the oceans are very efficient at conducting of sound, especially at frequencies of less than a few hundred hertz.

There are two major advantages in measuring the temperature using acoustic tomography. The first one is the capability of measuring large areas of the ocean's interior by remote sensing and the second one is that the technique gives the averages of the fluctuations of temperature at small scales that are the main reasons

behind the variations in the oceans.

Reciprocal tomography could also be employed in the ocean acoustic tomography measurements. In reciprocal tomography the transmissions are done, instead of a single source and a single receiver, using two acoustic transceivers. These acoustic transceivers are devices that could work both as source and as a receiver of the signal. The transmissions are performed simultaneosly with both of the transceivers. Ocean currents could be measured based on the slight differences in the travel times of these two signals as one them travels with and another against the current. The measure of temperature is the average of these two travel times. This way the small effects to the travel times caused by the ocean currents could be removed. However, the ocean currents generally affect the travel times much less than the variations in the speed of sound, hence the one-way tomography is enough to measure the temperature to good approximation [25] [12].

3. MATHEMATICS

The mathematical steps of this work are presented in this chapter. The whole prodecure aims at recovering the permittivy in a spatial domain. First the forward model for the electric potential is introduced. Then the definitions of gradient and partial derivative of the potential leads to first order system. Then it is explained how one can obtain the weak formulation for this first order system by using test functions and integrating by parts.

Then discretization of the spatial domain with finite elements applying the Ritz-Galerkin method produces the weak formulation as system of linear equations. Temporal discretization of this system then leads to a leap-frog time integration system that is utilized in simulation of the signal in the original domain.

This system is then differentiated in order to simulate the differentiated signal. Deconvolution method and the reciprocity of the wave propagation are employed in computations of both the actual and the differentiated signal. Multiresolution and incomplete Cholesky decomposition are used to speed up the computation. Finally this leads to an inversion problem from which the permittivities of the target objects are recovered using variation regularized iterative procedure.

3.1 Forward model

The forward model is used to predict the electric potential in the set [0, T] $\times$ Ω. In this set [0, T] is the time interval and Ω is the spatial domain that consists of the target objects Ω_0 and the orbiter paths as well. The following hyperbolic wave equation could be written for the electric potential in this set when given a real-valued relative permittivity ε_r, real conductivity distribution σ and the initial conditions $\phi\,|_{t=0}= \phi_0$ and $(\partial\phi/\partial t)\,|_{t=0}= u_1$:

$$\varepsilon_r \frac{\partial^2 \phi}{\partial t^2} + \sigma \frac{\partial \phi}{\partial t} - \Delta_{\vec{x}} \phi = \frac{\partial f}{\partial t} \qquad \text{for all} \qquad (t, \vec{x}) \in [0, T] \times \Omega \tag{3.1}$$

The right hand side of this equation presents a signal $f(t, \vec{x}) = \tilde{f}(t)\delta_{\vec{p}}(\vec{x})$ that is

transmitted at point $\vec{p}$, in which $\tilde{f}(t)$ stands for the time-dependent part of the signal and $\delta_{\vec{p}}(\vec{x})$ for a Dirac's delta function with respect to point $\vec{p}$. The symbol Δ here is a laplace operator that is by its definition the divergence of a gradient. In this case this means that the last term on the left hand side can be written as $\Delta = \nabla \cdot \nabla\phi$. Let us then define $\vec{g}$ as a gradient and u as partial derivative of the potental ϕ with respect to t i.e. $\vec{g} = \nabla\phi$ and $u = \partial\phi/\partial t$. By placing these definitions to equation (3.1) we get

$$\varepsilon_r \frac{\partial u}{\partial t} + \sigma u - \nabla \cdot \vec{g} = \frac{\partial f}{\partial t}, \tag{3.2}$$

and by taking the partial derivative of the definition of $\vec{g}$ with respect to t and placing u in this equation we get

$$\frac{\partial \vec{g}}{\partial t} - \nabla u = \mathbf{0}. \tag{3.3}$$

These two equations form a first order system in the set $\Omega \times [0, T]$. The definitions of $\vec{g}$ and u together with the initial conditions that were given before mean that $\vec{g} \mid_{t=0} = \nabla\phi_0, u \mid_{t=0} = u_1$ in this system. In order to get the weak formulation of this system we first multiplicate the equation (3.2) by test function $v : [0, T] \to H^1(\Omega)$ and the equation (3.3) by test function $\vec{w} : [0, T] \to L_2(\Omega)$. These test function are suitably chosen so that they satisfy the weak formulation of the system. The function space $L_2(\Omega)$ is a space that consists of all functions that are square-integrable over Ω in the sense of Lebesgue. The next step is to integrate these equations. For the third term of the first equation the integration needs to be done utilizing integration by parts. By definiton the formula for integration by parts is

$$\int_\Omega \frac{\partial v}{\partial x_i} g_i \, \mathrm{d}\Omega = \int_\Gamma v \, g_i \, n_i \, \mathrm{d}\Gamma - \int_\Omega v \frac{\partial g_i}{\partial x_i} \, \mathrm{d}\Omega. \tag{3.4}$$

Then summing over the indices i gives the vector formula

$$\int_\Omega \nabla v \cdot \vec{g} \, \mathrm{d}\Omega = \int_\Gamma v(\vec{g} \cdot \vec{n}) \, \mathrm{d}\Gamma - \int_\Omega v \, \nabla \cdot \vec{g} \, \mathrm{d}\Omega. \tag{3.5}$$

The vector $\vec{n}$ here is the outward unit surface normal to Γ. The term containing this vector vanishes as the propagated wave never gets outside of the domain Ω. Now when reading from right to left this equation gives the integral of the original term

that was multiplicated by test function v. Now we can write the weak formulation of the system.

$$\frac{\partial}{\partial t}\int_\Omega \vec{g}\cdot\vec{w}\ \mathrm{d}\Omega - \int_\Omega \vec{w}\cdot\nabla u\ \mathrm{d}\Omega = \mathbf{0} \tag{3.6}$$

$$\frac{\partial}{\partial t}\int_\Omega \varepsilon_r\ u\ v\ \mathrm{d}\Omega + \int_\Omega \sigma\ u\ v\ \mathrm{d}\Omega + \int_\Omega \vec{g}\cdot\nabla v\ \mathrm{d}\Omega = \begin{cases}\tilde{f}(t), & \text{if } \vec{x}=\vec{p},\\ 0, & \text{else.}\end{cases} \tag{3.7}$$

Under regular enough conditions the weak form has a unique solution $u : [0,T] \to H^1(\Omega)$, which also works as a unique solution to the original first order system. [26] The SI-unit values corresponding to t, $\vec{x}$, ε_r, σ and signal velocity $c = {\varepsilon_r}^{-1/2}$ can be obtained respectively via $(\mu_0\varepsilon_0)^{1/2}st, s\vec{x}, \varepsilon_0\varepsilon_r, (\varepsilon_0/\mu_0)^{1/2}s^{-1}\sigma$, and $(\varepsilon_0\mu)^{-1/2}c$. Here s is a suitably chosen scaling vector (meters) and the constants $\varepsilon_0 = 8.85\cdot 10^{-12}$ F/m and $\mu_0 = 4\pi\cdot 10^{-7}$ H/m.

3.2 Forward simulation

Ritz-Galerkin method is one way to find an approximate solution to a problem in weak form. The method is based on the idea that the spatial domain Ω can be discretized and the problem then be solved in the set that was produced by this discretization. The domain is here discretized using a set of finite elements (FEs) $\mathcal{T} = \{T_1, T_2, \ldots, T_m\}$ together with piecewise linear functions $\varphi_1, \varphi_2, \ldots, \varphi_n \in b^1(\Omega)$ that form the basis for this set. The basis functions are called nodal functions since each one of them corresponds to a specific node $\vec{r}_1, \vec{r}_2, \ldots, \vec{r}_n$ of the finite triangular mesh $\mathcal{T}$. As seen in the figure 3.1 the nodal function is a piecewise linear function that gets a value of one in one node of the mesh and is zero in other nodes.

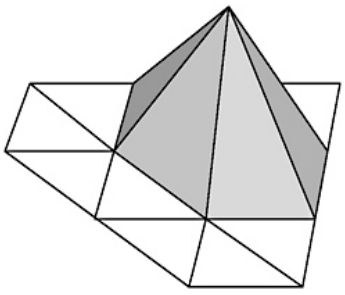

Figure 3.1 *Picture of nodal function, source: Finite Elements: Theory, Fast Solvers, and Applications in Elasticity Theory by Dietrich Braess*

The Ritz-Galerkin approximations of the potential and gradient fields are $u = \sum_{j=1}^{n} p_j \varphi_j$ and $\vec{g} = \sum_{k=1}^{d} g^{(k)} \vec{e}_k$, where d is the number of spatial dimensions (2 or 3) and $g^{(k)} = \sum_{i=1}^{m} q_i^{(k)} \chi_i$ is a sum of element indicator functions $\chi_1, \chi_2, \ldots, \chi_m \in L_2(\Omega)$. These element indicator functions are said to be piecewise constant as each of them gets a value of one only in the corresponding triangle of the finite triangular mesh and is zero everywhere else. This is illustrated in a figure 3.2.

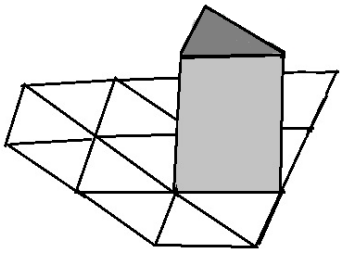

Figure 3.2 *Picture of element indicator function*

Definining the test functions $v : [0,T] \to \mathcal{V} \subset b^1(\Omega)$ and $\vec{w} : [0,T] \to \mathcal{W} \subset L_2(\Omega)$ with $\mathcal{V} = \text{span}\{\varphi_1, \varphi_2, \ldots, \varphi_n\}$ and $\mathcal{W} = \text{span}\{\chi_1, \chi_2, \ldots, \chi_m\}$ the Ritz-Galerkin method produces the weak formulation as a system of linear equations. [15]

$$\frac{\partial}{\partial t}\mathbf{A}\mathbf{q}^{(k)} - \mathbf{B}^{(k)}\mathbf{p} + \mathbf{T}^{(k)}\mathbf{q}^{(k)} = 0, \tag{3.8}$$

$$\frac{\partial}{\partial t}\mathbf{C}\mathbf{p} + \mathbf{R}\mathbf{p} + \mathbf{S}\mathbf{p} + \sum_{k=1}^{d} \mathbf{B}^{(k)^T}\mathbf{q}^{(k)} = \mathbf{f}, \tag{3.9}$$

where $\mathbf{p} = (p_1, p_2, \ldots, p_m)$, $\mathbf{q}^{(k)} = (q_1^{(k)}, q_2^{(k)}, \ldots, q_n^{(k)})$ and

$$A_{i,i} = \int_{T_i} \mathrm{d}\Omega, \qquad A_{i,j} = 0, \quad \text{if} \quad i \neq j, \tag{3.10}$$

$$f_i = \int_{\Omega} f\varphi_i \, \mathrm{d}\Omega, \quad B_{i,j}^{(k)} = \int_{T_i} \mathbf{e}_k \cdot \nabla\varphi_j \, \mathrm{d}\Omega, \tag{3.11}$$

$$C_{i,j} = \int_{\Omega} \varepsilon \, \varphi_i\varphi_j \, \mathrm{d}\Omega, \quad R_{i,j} = \int_{\Omega} \sigma\varphi_i\varphi_j \, \mathrm{d}\Omega, \tag{3.12}$$

$$S_{i,j} = \int_{\Omega} \xi \ \varphi_i \varphi_j \ \mathrm{d}\Omega, \quad T_{i,j}^{(k)} = \zeta^{(k)} A_{i,j}. \tag{3.13}$$

The Matrices $\mathbf{S}$ and $\mathbf{T}^k$ are additional and correspond to a split-field perfectly matched layer (PML). The PML is here defined for the outermost part of the computational domain $\{\vec{x} \in \Omega \mid \sigma_1 \leq \max_k |x_k| \leq \sigma_2\}$. The use of PML eliminates the reflections from the boundary $\partial\Omega$ back to the inner part of Ω [14]. Parameters ξ and ζ in the equation (3.13) are the absorption parameters. The first one is defined as

$$\begin{cases} \xi(\vec{x}) = \varsigma, \text{ if } \sigma_1 \leq \max_k |x_k| \leq \sigma_2 \\ \xi(\vec{x}) = 0 \text{ otherwise,} \end{cases} \tag{3.14}$$

and second one as

$$\begin{cases} \zeta^{(k)}(\vec{x}) = \varsigma, \text{ if } \sigma_1 \leq |x_k| \leq \sigma_2 \\ \zeta^{(k)}(\vec{x}) = 0 \text{ otherwise.} \end{cases} \tag{3.15}$$

The time interval [0, T] was discretized using the standard finite difference approach within a Δt spaced regular grid of N time points. A straightforward temporal discretization of the equations (3.8) and (3.9) produces the following equations that are called the leap-frop time integration system:

$$\mathbf{q}_{l+\frac{1}{2}}^{(k)} = \mathbf{q}_{l-\frac{1}{2}}^{(k)} + \Delta t \mathbf{A}^{-1} \left(\mathbf{B}^{(k)} \mathbf{p}_l - \mathbf{T}^{(k)} \mathbf{q}_{l-\frac{1}{2}}^{(k)} \right), \tag{3.16}$$

$$\mathbf{p}_{l+1} = \mathbf{p}_l + \Delta t \mathbf{C}^{-1} \left(\mathbf{f}_l - \mathbf{R}\mathbf{p}_l - \mathbf{S}\mathbf{p}_- \sum_{k=1}^{d} \mathbf{B}^{(k)^T} \mathbf{q}_{l+\frac{1}{2}}^{(k)} \right). \tag{3.17}$$

Here the charge is advanced using the first equation and the potential is advanced using the second equation. The former value of the potential is needed in calculating the value of the next charge and then the former value of the charge in turn is needed in calculating the next value of the potential. These steps are then repeated in order to calculate all the values of the potential and the charge. This system can be used to simulate a signal propagating in a domain Ω [14], [27], [28].

3.2.1 Differentiated signal

The permittivity ε_r is here expressed as a sum of two different terms in the form $\varepsilon_r = \varepsilon_r^{(bg)} + \varepsilon_r^{(p)}$, where the first term $\varepsilon_r^{(bg)}$ represents a fixed background permittivity distribution and the second term $\varepsilon_r^{(p)} = \sum_{j=1}^{n} c_j \chi_j^{'}$ is a variable perturbation composed by indicator functions of a coarse mesh $\mathcal{T}' = \{T_1^{'}, T_2^{'}, \ldots, T_M^{'}\}$. The resolution of $\mathcal{T}^{'}$ is here chosen due to targeted precision of the inversion results whereas the density of $\mathcal{T}$ is restricted by the geometrical constraints of the forward model such as the structure of the domain and the applied wavelength. The meshes $\mathcal{T}$ and $\mathcal{T}'$ are here presumed to be nested which means that the nodes of $\mathcal{T}'$ are also included in the nodes of $\mathcal{T}$. Differentiating the equations (3.16),(3.17) with respect to c_j at $\varepsilon_r = \varepsilon_r^{(bg)}$ leads to following equations

$$\frac{\partial \mathbf{q}_{l+\frac{1}{2}}^{(k)}}{\partial c_j} = \frac{\partial \mathbf{q}_{l-\frac{1}{2}}^{(k)}}{\partial c_j} + \Delta t \mathbf{A}^{-1} \left(\mathbf{B}^{(k)} \frac{\partial \mathbf{p}_l}{\partial c_j} - \mathbf{T}^{(k)} \frac{\partial \mathbf{q}_{l-\frac{1}{2}}^{(k)}}{\partial c_j} \right), \tag{3.18}$$

$$\begin{aligned} \frac{\partial \mathbf{p}_{l+1}}{\partial c_j} =& \frac{\partial \mathbf{p}_l}{\partial c_j} - \Delta t \mathbf{C}^{-1} \left(\mathbf{R} \frac{\partial \mathbf{p}_l}{\partial c_j} + \mathbf{S} \frac{\partial \mathbf{p}_l}{\partial c_j} + \sum_{k=1}^{d} \mathbf{B}^{(k)} \frac{\partial \mathbf{q}_{l+\frac{1}{2}}^{(k)}}{\partial c_j} \right) \\ & - \Delta t \frac{\partial \mathbf{C}^{-1}}{\partial c_j} \sum_{k=1}^{d} \mathbf{B}^{(k)^T} \mathbf{q}_{l+\frac{1}{2}}^{(k)} \end{aligned} \tag{3.19}$$

The matrix $\partial \mathbf{C}^{-1} / \partial c_j$ in the last term of the equation (3.19) can be expressed as $\partial \mathbf{C}^{-1} / \partial c_j = -\mathbf{C}^{-1} (\partial \mathbf{C} / \partial c_j) \mathbf{C}^{-1}$. This could be obtained by straightforwad differentiation of the identity $\mathbf{C}\mathbf{C}^{-1} = \mathbf{I}$.

$$\frac{\partial (\mathbf{C}\mathbf{C}^{-1})}{\partial c_j} = \frac{\partial \mathbf{C}}{\partial c_j} \mathbf{C}^{-1} + \frac{\partial \mathbf{C}^{-1}}{\partial c_j} \mathbf{C} = \mathbf{0} \tag{3.20}$$

The derivative of the identity matrix is always a zero matrix. Now switching the first term to the right hand side and dividing by the matrix $\mathbf{C}$ we get

$$\frac{\partial \mathbf{C}^{-1}}{\partial c_j} = -\mathbf{C}^{-1} \frac{\partial \mathbf{C}}{\partial c_j} \mathbf{C}^{-1} \tag{3.21}$$

with

$$\left[\frac{\partial \mathbf{C}}{\partial c_j} \right]_{i_1, i_2} = \int_{T_j^{'}} \varphi_{i_1} \varphi_{i_2} \mathrm{d}\Omega \tag{3.22}$$

if the j-th elementh includes the nodes i_1 and i_2 and otherwise $[\partial \mathbf{C}/\partial c_j]_{i_1,i_2} = 0$. The second equation then takes the form:

$$\begin{aligned}\frac{\partial \mathbf{p}_{l+1}}{\partial c_j} =& \frac{\partial \mathbf{p}_l}{\partial c_j} + \Delta t \mathbf{C}^{-1} \left(\mathbf{R}\frac{\partial \mathbf{p}_l}{\partial c_j} + \mathbf{S}\frac{\partial \mathbf{p}_l}{\partial c_j} + \sum_{k=1}^{d} \mathbf{B}^{(k)} \frac{\partial \mathbf{q}_{l+\frac{1}{2}}^{(k)}}{\partial c_j} \right) \\ &+ \Delta t \mathbf{C}^{-1} \frac{\partial \mathbf{C}}{\partial c_j} \mathbf{C}^{-1} \sum_{k=1}^{d} \mathbf{B}^{(k)^T} \mathbf{q}_{l+\frac{1}{2}}^{(k)}.\end{aligned} \tag{3.23}$$

And defining $\mathbf{b} = \mathbf{C}^{-1} \sum_{k=1}^{d} \mathbf{B}^{(k)^T} \mathbf{q}^{(k)}$ the whole system can be written in the following form.

$$\frac{\partial \mathbf{q}_{l+\frac{1}{2}}^{(k)}}{\partial c_j} = \frac{\partial \mathbf{q}_{l-\frac{1}{2}}^{(k)}}{\partial c_j} + \Delta t \mathbf{A}^{-1} \left(\mathbf{B}^{(k)} \frac{\partial \mathbf{p}_l}{\partial c_j} - \mathbf{T}^{(k)} \frac{\partial \mathbf{q}_{l-\frac{1}{2}}^{(k)}}{\partial c_j} \right), \tag{3.24}$$

$$\frac{\partial \mathbf{p}_{l+1}}{\partial c_j} = \frac{\partial \mathbf{p}_l}{\partial c_j} + \Delta t \mathbf{C}^{-1} \left(\frac{\partial \mathbf{C}}{\partial c_j} \mathbf{b}_l - \mathbf{R}\frac{\partial \mathbf{p}_l}{\partial c_j} - \mathbf{S}\frac{\partial \mathbf{p}_l}{\partial c_j} - \sum_{k=1}^{d} \mathbf{B}^{(k)^T} \frac{\partial \mathbf{q}_{l+\frac{1}{2}}^{(k)}}{\partial c_j} \right) \tag{3.25}$$

The last equation is now almost equal to (3.17) but it has as a source $(\partial \mathbf{C}/\partial c_j)\mathbf{b}$ that is specific to the j-th element in the FE mesh $\mathcal{T}'$. The differentiated potential can be computed as the sum $\partial \mathbf{p}/\partial c_j = \sum_{i=1}^{n} \mathbf{d}^{(i,j)}$ since the node-specific form $(\partial \mathbf{C}/\partial c_j)\mathbf{b}^{(i)}$ satisfies $(\partial \mathbf{C}/\partial c_j)\mathbf{b} = \sum_{i=1}^{n} (\partial \mathbf{C}/\partial c_j)\mathbf{b}^{(i)}$ and because of the linearity of the wave equation. The terms can be obtained through equations(3.18),(3.19). The vector $(\partial \mathbf{C}/\partial c_j)\mathbf{b}^{(i)}$ here is nonzero only if the i-th node belongs to $T_j' \in \mathcal{T}'$, since the sparse structure of both $(\partial \mathbf{C}/\partial c_j)$ and $\mathbf{b}^{(i)}$. Then by defining

$$\mathbf{h}^{(i,j)} = \frac{\partial \mathbf{C}}{\partial c_j} \mathbf{b}^{(i)}, \qquad \text{with} \begin{cases} b_j^{(i)} = b_i, \text{ if } j = i \\ b_j^{(i)} = 0 \text{ otherwise} \end{cases} \tag{3.26}$$

the differentiated potential can be computed as the sum $\partial \mathbf{p}/\partial c_j = \sum_{\vec{r} \in \mathcal{T}_j'} \mathbf{d}^{(i,j)}$. The terms of the sum can be calculated through the following system

$$\mathbf{r}_{l+\frac{1}{2}}^{(i,j,k)} = \mathbf{r}_{l-\frac{1}{2}}^{(i,j,k)} + \Delta t \mathbf{A}^{-1} \left(\mathbf{B}^{(k)} \hat{\mathbf{p}}_l^{(i,j)} - \mathbf{T}^{(k)} \mathbf{r}_{l-\frac{1}{2}}^{(i,j,k)} \right), \tag{3.27}$$

$$\mathbf{d}_{l+1}^{(i,j)} = \mathbf{d}_{l}^{(i,j)} + \Delta t \mathbf{C}^{-1} \left(\mathbf{h}^{(i,j)} - \mathbf{R}\hat{\mathbf{p}}_{l}^{(i,j)} - \mathbf{S}\mathbf{d}_{l}^{(i,j)} - \sum_{k=1}^{d} \mathbf{B}^{(k)^T} \mathbf{r}_{l+\frac{1}{2}}^{(i,j,k)} \right). \tag{3.28}$$

In this system the node-specific vector $\mathbf{h}^{(i,j)} = (\partial \mathbf{C}/\partial c_j)\mathbf{b}^{(i)}$ is working as a source whereas in the first system the source term was $\mathbf{f}$. Since computation of $\mathbf{p}$ needs to be done before computation of $\mathbf{b}^{(i)}$ the source term $\mathbf{h}^{(i,j)}$ that corresponds to the actual potential $\mathbf{p}$ is here identicated as the primary one and the source term $\mathbf{f}$ that corresponds to the differentiated potential $\partial \mathbf{p}/\partial c_j$ as the secondary one. It is explained in the next section how the computation of the signal transmitted by the secondary source can be done using deconvolution and the reciprocity of the propagating wave [29].

3.2.2 Signal reciprocity and deconvolution

If transmission of a infinitely short monopolar pulse $\delta(t)\delta_{\vec{a}}(\vec{x})$ from point $\vec{a}$ results in receiving data $\mathcal{G}_{\vec{a},\vec{b}}(t)$ at point $\vec{b}$ then an abritrary transmission $\tilde{h}(t)$ made at point $\vec{a}$ leads to data $\tilde{d}(t)$ received at point $\vec{b}$. The received data $\tilde{d}(t)$ obeys the linear convolution relation:

$$\tilde{d}(t) = \mathcal{G}_{\vec{a},\vec{b}} *_t \tilde{h}(t) = \int_{-\infty}^{\infty} \mathcal{G}_{\vec{a},\vec{b}}(t-\tau)\tilde{h}(\tau)\mathrm{d}\tau, \tag{3.29}$$

due to the linearity of the wave equation with respect to the source and since $\tilde{h}(t) = \tilde{h} *_t \delta(t)$ at point $\vec{a}$. A regularized deconvolution procedure can be used to approximate the Green's kernel $\mathcal{G}_{\vec{a},\vec{b}}$ based on equation (3.29). Due to reciprocity of a propagating wave, the Green's kernel between the points $\vec{a}$ and $\vec{b}$ is equal to the Green's kernel between the points $\vec{a}$ and $\vec{b}$, so $\mathcal{G}_{\vec{a},\vec{b}} = \mathcal{G}_{\vec{b},\vec{a}}$. Therefore, another signal $\tilde{f}(t)$ transmitted from point $\vec{b}$ leads to data $\tilde{p}(t) = \mathcal{G}_{\vec{b},\vec{a}} *_t \tilde{f}(t)$ received at point $\vec{a}$. This transmission-receival pair $\tilde{f}(t), \tilde{p}(t)$ together with the previous pair $\tilde{d}(t), \tilde{h}(t)$ can be used in the following deconvolution process.

Let $\tilde{d}^{(i,j)}$ now be the N-by-1 time evolution of $\mathbf{d}^{(i,j)}$ at point $\vec{p_2}$ and to be computed based on a monopolar transmission $\tilde{\mathbf{f}}$ made at point $\vec{p_1}$. Let $\tilde{\mathbf{p}}$ and $\tilde{\mathbf{h}}^{(i,j)}$ be the time evolutions of $\mathbf{p}$ and $\mathbf{h}^{(i,j)}$ at a node $\vec{r} \in T_j'$ with sources placed at points $\vec{p_1}$ and $\vec{p_2}$. The time evolution $\tilde{\mathbf{d}}^{(i,j)}$ can now be obtained through these three steps and by repeating them for each node $\vec{r} \in T_j'$ (3.3):

1) Approximate the Green's kernel between $\vec{r}$ and $\vec{p_2}$ in the following Tikhonov

regularized form

$$\tilde{\mathbf{g}} = [\mathbf{K}_{\tilde{\mathbf{f}}}^T \mathbf{K}_{\tilde{\mathbf{f}}} + \nu \mathbf{I}]^{-1} \mathbf{K}_{\tilde{\mathbf{f}}}^T \begin{pmatrix} \mathbf{0} \\ \tilde{\mathbf{p}} \\ \mathbf{0} \end{pmatrix} \tag{3.30}$$

where

$$\mathbf{K}_{\tilde{\mathbf{f}}} = \begin{pmatrix} \tilde{f}_1 & 0 & 0 & 0 & 0 \\ \tilde{f}_2 & \tilde{f}_1 & 0 & 0 & 0 \\ \vdots & \tilde{f}_2 & \ddots & 0 & 0 \\ \tilde{f}_N & \vdots & \ddots & \tilde{f}_1 & 0 \\ 0 & \tilde{f}_N & & \tilde{f}_2 & \tilde{f}_1 \end{pmatrix}, \tag{3.31}$$

and ν is a regularization parameter, $\mathbf{0}$ is a N-by-1 zero-continuation of the signal and $\mathbf{K}_{\tilde{\mathbf{f}}}$ is a $3N$-by-$3N$ convolution matrix.

2) Compute the convolution $\tilde{\mathbf{d}} = \mathbf{P}\mathbf{K}_{\tilde{\mathbf{h}}}\tilde{\mathbf{g}}$ between $\tilde{\mathbf{g}}$ and $\tilde{\mathbf{h}}$. The matrix $\mathbf{P}$ here picks the centermost N entries of a $3N$-by-1 vector.

3) Update $\tilde{\mathbf{d}}^{(i,j)} = \tilde{\mathbf{d}}^{(i,j)} + \tilde{\mathbf{d}}$.

The main reason to use this kind of approach is that it allows rapid computation of the differentiated signal $\partial\mathbf{p}/\partial c_j$ for each element of the mesh $\mathcal{T}_j$, $j = 1, 2, \ldots, M$ by propagating two waves through the leap-frog system expressed in the equations (3.16)(3.17):

1) $\mathbf{b}$ with $\mathbf{f}$ transmissed at $\vec{p_1}$
2) $\mathbf{p}$ with $\mathbf{f}$ transmissed at $\vec{p_2}$.

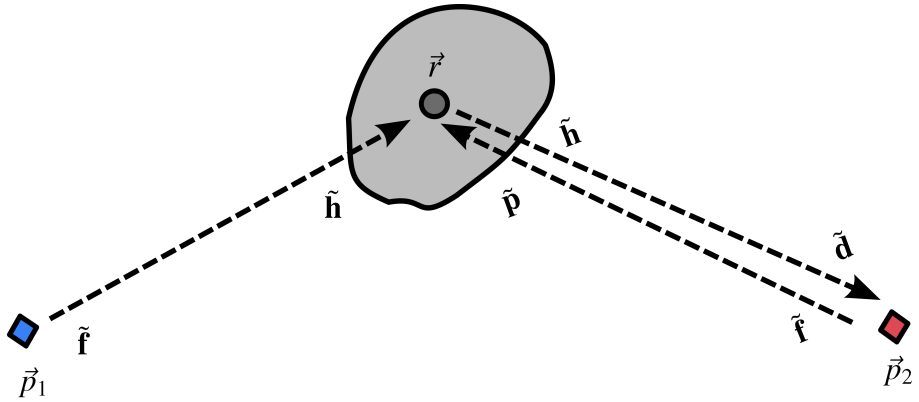

Figure 3.3 *A picture that demonstrates the steps in computation of* $\tilde{\mathbf{d}}$ *that is the time evolution of* $\mathbf{d}^{(i,j)}$ *at the receival point* $\vec{p_2}$ *as a result of a transmission of signal* $\tilde{\mathbf{f}}$ *at point* $\vec{p_1}$*. The following four-step procedure is used: (1) Compute* $\tilde{\mathbf{p}}$ *at* $\vec{r}$ *when the source* $\tilde{\mathbf{f}}$ *is placed at* $\vec{p_2}$*. (2) Approximate the Green's kernel* $\tilde{\mathbf{g}}$ *between* $\vec{r}$ *and* $\vec{p_2}$*. (3) Calculate* $\tilde{\mathbf{h}}$ *at* $\vec{r}$ *resulting from transmission of* $\tilde{\mathbf{f}}$ *at* $\vec{p_1}$*. (4) Compute* $\tilde{\mathbf{d}}$ *as the convolution between* $\tilde{\mathbf{g}}$ *and* $\tilde{\mathbf{h}}$*.*

3.3 Multiresolution computation

The forward simulation process can be speeded up by using multiresolution approach instead of single resolution one. With multiresolution the number of terms in the sum $\partial \mathbf{p}/\partial c_j = \sum_{\vec{r_i} \in T_j'} \mathbf{d}^{(i,j)}$ is reduced by defining the system (3.18)(3.19) for the coarse mesh $\mathcal{T}'$ instead of $\mathcal{T}$. The vectors $\mathbf{b}$ and $\mathbf{p}$ needed for finding $\mathbf{d}^{(i,j)}$ are still produced using the mesh $\mathcal{T}$ since the resolution of the coarse mesh $\mathcal{T}'$ is too low for propagating a wave. As mentioned before these two meshes are assumed to be nested meaning that the degrees of freedom i.e. the node values for the mesh $\mathcal{T}'$ are included to the node values of mesh $\mathcal{T}$. This means that the vectors $\mathbf{b}$ and $\mathbf{p}$ can be transferred to the basis of $\mathcal{T}'$ via a direct restriction, similar to the multigrid approaches [15]. From the memory consumption viewpoint it is advantageous that only the subvectors of $\mathbf{b}$ and $\mathbf{p}$ need to be accessed during the computation.

To obtain further speedup and memory saving in the leap-frog integration the incomplete Cholesky factorization together with the symmetric approximate minimum degree permutation of the entries were used in decomposition of the mass matrix $\mathbf{C}$.

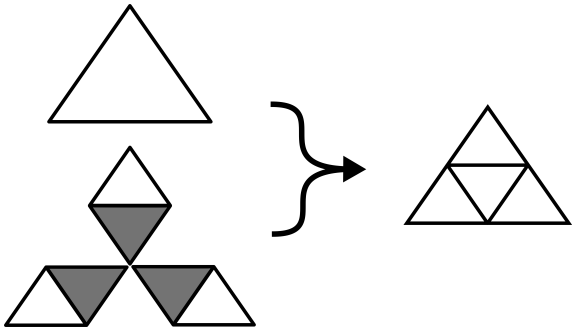

Figure 3.4 *Illustration showing how the denser mesh is formed from the sparser mesh and three wavelets with the multiresolution approach.*

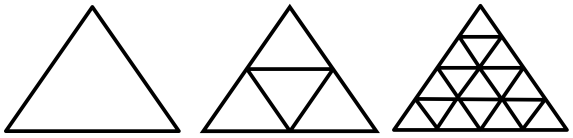

Figure 3.5 *Three triangular finite element meshes with different resolutions.*

3.4 Inverse problem

Permittivity can here be recovered in both single and multiresolution cases using the following formula

$$\mathbf{L}\mathbf{x} + \mathbf{n} = \mathbf{y} - \mathbf{y}_{bg}, \tag{3.32}$$

where $\mathbf{y}$ is a vector containing the actual data, $\mathbf{y}_{bg}$ a vector containing the simulated data for the background permittivity, $\mathbf{L}$ a matrix containing the differentiated signal and $\mathbf{n}$ is a noise term containing possible errors in modeling and measurement. The estimate for $\mathbf{x}$ is to be produced by using two slightly different iterative regularization procedures.

3.4.1 Single resolution inversion

With single resolution approach the inversion procedure is the following

$$\mathbf{x}_{l+1} = (\mathbf{L}^T\mathbf{L} + \boldsymbol{\alpha}_l\mathbf{D}\boldsymbol{\Gamma}_l\mathbf{D})^{-1}\mathbf{L}^T\mathbf{y}, \tag{3.33}$$

where $\mathbf{\Gamma}_l = \text{diag}(|\mathbf{D}\mathbf{x}_l|)^{-1}$, with $\mathbf{\Gamma}_0 = \mathbf{I}$ for $l = 1, 2, \ldots$ and $\boldsymbol{\alpha}_l = \|\mathbf{\Gamma}_l\|/\text{length}(\mathbf{x})$ with $\boldsymbol{\alpha}_0$ changing in different cases. The matrix $\mathbf{D}$ is of the form

$$D_{i,j} = \beta\delta_{i,j} + \frac{\int_{T_i' \cap T_j'}(2\delta_{i,j} - 1)ds}{\max_{i,j}\{\int_{T_i' \cap T_j'} ds\}}, \quad \text{where} \quad \delta_{i,j} = \begin{cases} 1, & \text{if} \quad j = i, \\ 0, & \text{otherwise.} \end{cases} \tag{3.34}$$

The first term is a weighted identity operator that limits the total magnitude of $\mathbf{x}$ and the second term penalizes the jumps of $\mathbf{x}$ over the edges of mesh $\mathcal{T}'$ multiplied with the edge length.

3.4.2 Multiresolution inversion

With multiresolution approach the steps of the iteration procedure are a bit more complicated. One iteration step can be divided into two steps. The estimate for $\mathbf{x}$ is achieved by computing estimates for two auxiliary parameters. In first step for parameter $\mathbf{x}_0$ and then in the second step for parameter $\mathbf{x}_1$.

The equation (3.35) used to compute the values of $\mathbf{x}_0$ is pretty much similar to the equation (3.33) but instead of matrix $\mathbf{D}$ it includes matrix $\mathbf{D}_0 = \mathbf{D}\mathbf{P}_c$ and instead of matrix $\mathbf{L}$ includes matrix $\mathbf{L}_0$. Both of these new matrices have only one quarter of the number of elements compared to the previous ones.

$$\mathbf{x}_{0,l+1} = (\mathbf{L}_0^T\mathbf{L}_0 + \boldsymbol{\alpha}\mathbf{D}_0\mathbf{\Gamma}_l\mathbf{D}_0)^{-1}\mathbf{L}_0^T\mathbf{y}, \tag{3.35}$$

Then for the second step only one third of the values of $\mathbf{x}_0$ are chosen based on the highest absolute values. Then matrices $\mathbf{L}_1$ and $\mathbf{D}_1$ are transformed from matrices $\mathbf{L}$ and $\mathbf{D}$ using matrix $\mathbf{P}_r$ that picks only the entries that correspond to the values of $\mathbf{x}_0$ that were chosen before. Also new vector $\mathbf{y}_0 = \mathbf{L}_0\mathbf{x}_0$ is computed.

$$\mathbf{x}_{1,l+1} = (\mathbf{L}_1^T\mathbf{L}_1 + \boldsymbol{\alpha}_l\mathbf{D}_1\mathbf{\Gamma}_l\mathbf{D}_1)^{-1}(\mathbf{L}_1^T\mathbf{y} - \mathbf{L}_1^T\mathbf{y}_0), \tag{3.36}$$

In every iteration step after computing either value of $\mathbf{x}_0$ or $\mathbf{x}_1$ the value of $\mathbf{x}$ is updated using the following formula:

$$\mathbf{x}_{l+1} = \mathbf{P}_c\mathbf{x}_{0,l+1} + \mathbf{P}_r\mathbf{x}_{1,l+1}. \tag{3.37}$$

Parameters $\mathbf{\Gamma}$ and $\boldsymbol{\alpha}$ are also updated after every step using the same formula as in the multiresolution case.

In both cases the above inversion processes minimize the function

$$F(\mathbf{x}) = \|\mathbf{L}\mathbf{x} - \mathbf{y}_{bg} - \mathbf{y}\|_2 + \|\mathbf{D}\mathbf{x}\|_1 \tag{3.38}$$

in which the second term equals to the total variation of $\mathbf{x}$, if $\beta = 0$. [30], [31], [1]. The above inversion procedure could then be regularized even more using classical 1-norm regularization [32], [33], [1] by transforming $\tilde{\mathbf{x}} = \mathbf{D}\mathbf{x}$ and $\tilde{\mathbf{L}} = \mathbf{L}\mathbf{D}^{-1}$. The iterative procedure could now be written as

$$\tilde{\mathbf{x}}_{l+1} = (\tilde{\mathbf{L}}^T\tilde{\mathbf{L}} + \boldsymbol{\alpha}_l\mathbf{\Gamma}_l)^{-1}\tilde{\mathbf{L}}^T\mathbf{y}, \tag{3.39}$$

where $\mathbf{\Gamma}_l = \mathrm{diag}(|\tilde{\mathbf{x}}_l|)^{-1}$, and $\mathbf{\Gamma}_0 = \mathbf{I}$.

4. NUMERICAL EXPERIMENTS

4.1 Permittivity

The permittivity distribution consisted of three elongated inclusions modeling vacuum cavities within Ω_0 along with a surface layer with thickness 10 % of the diameter of Ω_0, e.g., dust or ice cover. The relative permittivity of the cavities was chosen to be one which is the same as the permittivity of a vacuum. Same value was also chosen for the exterior of Ω. In other parts of the domain the permittivity was assumed to be granular the grain (finite element) size being 0.3-1.5 m (0.00060-0.0030). For the surface layer the permittivity of each grain was drawn from a uniform distribution covering the interval [1, 3] and for the rest of the domain from an uniform distribution covering the interval [2, 6].

The background permittivity of Ω_0, i.e., the initial guess of the inversion procedure, was chosen to be 4, that matches the permittivity of granite [34], [35], [36]. Vacuum background permittivity 1 was used for the remaining subdomain.

4.2 Conductivity

The conductivity that causes the energy loss in the signal was assumed to have a latent distribution $\sigma = 5\epsilon_r$ in the subdomain Ω_0. That is around 0.11 m S/m or 0.003 dB/m attenuation with the background permittivity value $\epsilon_r = 4$. The other parts of the domain i.e. $\Omega \backslash \Omega_0$ were assumed to be lossless i.e. $\sigma = 0$ The a priori guesses used in the forward simulation were $\sigma = 20$ in Ω_0 and $\sigma = 0$ in the exterior of Ω_0

4.3 Signal

The signal $\partial f/\partial t$ with $f(t, \vec{x}) = \tilde{f}(t))\delta_{\vec{p}}(\vec{x})$ transmitted in 3.1 was determined by Blackman-Harris window [37], [38], [39]

$$\tilde{f}(t) = 0.359 - 0.488cos(20\pi t) + 0.141cos(40\pi t) - 0.012cos(60\pi t) \tag{4.1}$$

for $t \leq 0.1$, and $\tilde{f}(t) = 0$ otherwise. The frequency of the signal was centered around 10 MHz. The data were gathered covering the time window from $t = 0$ to $T = 1.3$ using 60 MHz frequency.

Numerical experiments were performed for 3 different types of signal configurations. These configurations are expressed in figure 4.1 and the specifications of these configurations are given in table 4.1. The number of transmitter satellites was three for the each of these configurations and it was assumed that the these satellites did not move so their relative orbital velocity was zero. The signal was recorded at each time step for configurations (A), after every fourth step for configuration (B) and after every eight time step for configuration (C). This gives a total number of 128 receivers for configuration (A), 32 for configuration (B) and 16 for configuration (C). The inversions were computed for everyone of these configurations using both the single and the multiresolution approach.

Configuration	(A)	(B)	(C)
Number of transmitters	3	3	3
Number of receiver positions	128	32	16
Receiver spacing	$\frac{\pi}{64}$	$\frac{\pi}{16}$	$\frac{\pi}{8}$
Time steps between signal recordings	1	4	8

Table 4.1 *Specifications of the signal configurations (A) - (C)*

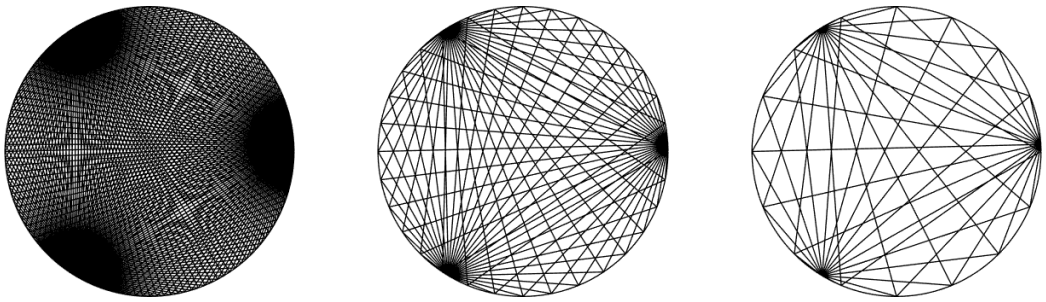

(A) (B) (C)

Figure 4.1 *Configurations (A) - (C) of the paths of the signal between transmission and receival points.*

4.4 Noise

The noise term in the formula (3.32) was presumed to consist of forward errors and simulated measurent nose. These possible forward inaccuracies could at least be categorized to modelling and simulation errors. The former of these could be

associated with the initial guess and the latter follows from the FDTD/FEM computations. The simulated measurement noise was produced using additive Gaussian white noise with mean value of zero and standard deviation of 6% wtih respect to the peak value of the signal at the measurement point. Most of the simulated noise peaks stayed at least 20dB below the main signal peak.

4.5 Forward computations

The exact data were computed using a different FE mesh (24881 nodes, 49360 triangles) than $\mathcal{T}$ of the forward simulation (24480 nodes, 48558 triangles) to avoid inversion crime [1], [40]. The temporal increment was chosen to be $\Delta t = 2.5 \cdot 10^{-4}$ in the leapfrog time integration process. The coarse mesh $\mathcal{T}'$ that covered the domain Ω_0 consisted of 6271 nodes and 12340 triangles in a way that Each element of $\mathcal{T}$ covers four triangles of $\mathcal{T}$ that follows from the refinement of the denser mesh.

4.6 Regularization

Regularization parameter $\nu = 10^{-7}$ needed in the deconvolution formula (3.30) was chosen in order to find the most feasible balance between accuracy and numerical stability of the estimates. Six different values $\{10^{-4}, 10^{-3}, 10^{-2}, 10^{-1}, 1, 10\}$ were tested for both parameters α and β that were needed in the inversion prodedures (3.33), (3.35) and (3.36) in order to find the most suitable combination and to compare the results.

4.7 Accuracy

The accuracy of these inversion procedures were measured by three different types of methods. First by computing relative overlapping areas (ROA) separately for the void and the cover and for the whole area as well. Then by computing the error of the values for void, cover and the whole area. Finally also total variations (TV) were calculated for the whole reconstructed data.

4.7.1 Error of relative overlap

One way to examine the accuracy of the inversion process is to use the relative overlapping area (ROA). It is here defined as follows

$$1 - \frac{\text{Area}(\mathcal{A})}{\text{Area}(\mathcal{S})}, \tag{4.2}$$

where $\mathcal{A} = \mathcal{S} \cap \mathcal{R}$ is the overlapping area of the sets $\mathcal{S}$ and $\mathcal{R}$. In which $\mathcal{S}$ is the area to be recovered and $\mathcal{R}$ the reconstructed area. Relative overlap was here computed separately for the cover and the void as well as for the whole area.

4.7.2 Error of the value

Another way to measure the accuracy of the inversion is to use the error of the value. It is defined as

$$\left| 1 - \frac{\sum \hat{\mathbf{x}}}{\sum \mathbf{x}} \right| \tag{4.3}$$

where $\sum \hat{\mathbf{x}}$ is the sum of the estimates of the permittivity distribution and $\sum \mathbf{x}$ is the sum of the real valued permittivity distribution i.e. the equation above expresses how much the estimated values differ from the the real ones on the average.

4.7.3 Total variation

Third way to measure the accuracy of the inversion is to calculate the total variation of it. It is here defined as the norm of the multiplication between matrix $\mathbf{D}$ and vector $\hat{\mathbf{x}}$.

$$\text{TV} = 10 \cdot \log_{10} \|\mathbf{D}\hat{\mathbf{x}}\|, \tag{4.4}$$

where $\mathbf{D}$ is the matrix defined before and $\hat{\mathbf{x}}$ is the estimate vector for $\mathbf{x}$. The values of total variatons differ largely depending on the choice of parameters and configuration so it might also be possible to express them using logarithmic decibel scale.

4.8 Robustness

The robustness of these calculations were inspected by calculating the mean values for every configuration and for both resolutions. This was done by summing up the errors of relative overlap and the errors of values for each case individually and then computing the average of these values for each case.

5. RESULTS

The results of the numerical experiments are gathered in this section. Figure 5.1 express the error of the relative overlap and the error of the value for the dense configuration (A) in both multi- and single resolution cases whereas figures 5.2 and 5.3 illustrate the same for the medium configuration (B) and the sparse configuration (C) respectively. This means that the smaller the value the better the approximation. In graphs this means that relative overlap and value are better in the darker areas and worse in the lighter areas. Total variations of each case are shown in figure 5.4. In each of those figures the values of parameter α are on the x-axis and the values of β on the y-axis.

For the robustness analysis that is illustrated in figure 5.5 the average values of the errors of overlap (cover, void, all) and the errors of the value (cover, void, all) were computed for each of the three configurations (A), (B) and (C). In the graphs on the x-axis is a percentage threshold that was chosen to run from 5% to 100% with steps of 5 percentage points and on the y-axis the percentage of the average values that are below that chosen threshold. In each of the three graphs the green colored curve presents the single resolution approach and the dark grey colored curve the multiresolution approach.

5.1 Error of relative overlap

For each configuration (A), (B) and (C) the graphs of the multi- and single resolution approaches have a strong resemblance between them. Although for every configuration the single resolution approach seemed to give slightly better ROA results for the whole area than the multiresolution approach. Between the configurations the results were the best for the dense configuration (A) and the worst for the sparse configuration (C) as was expected. Configurations (A) and (B) came out be more suitable for reconstructing the cover than the void whereas configuration (C) was more suitable for reconstructing the void than the cover.

The choice of parameters α and β altered highly to results with every configuration using both single and multiresolution approach. The choice of α seemed to have

greater effect on the results than the choice of β. With every configuration and resolution the best results where achieved using some combination of the values $\{0.01, 0.1, 1\}$ for α and the values $\{0.0001, ..., 1\}$ for β. The smallest and the highest values of α combined with any values of β and the combination of the highest values of β with any values of α did not give that good results.

5.2 Error of value

With each configuration and both resolution approachess the results were significantly better for cover than void if the error of the value was used as a measure. The errors of the values for void were smaller when both parameters α and β were chosen to be small and bigger when both parameters were chosen to be big. For the cover the smallest erros of values were achieved when both parameters were chosen from somewhere in the middle. The errors of the values were at their largest when both parameters was chosed to be either very small or very large. For the whole area the best results were gained using relatively small values for both parameters but there could not be seen such a clear pattern as there there were with void and cover independently. Only the combination of large values of both parameters gave explicitly worse results.

With every three configuration the absolute best results were achieved with multiresolution when the parameters could be chosen accurately. Single resolution turned out to be more flexible to the choice of the parameters as the results were relatively good with larger scale of parameters. This held true for void, cover and whole area as well. Between the configurations the errors of values were the smaller the more dense was the configuration. Which means that configuration (A) was the best and configuration (C) was the worst.

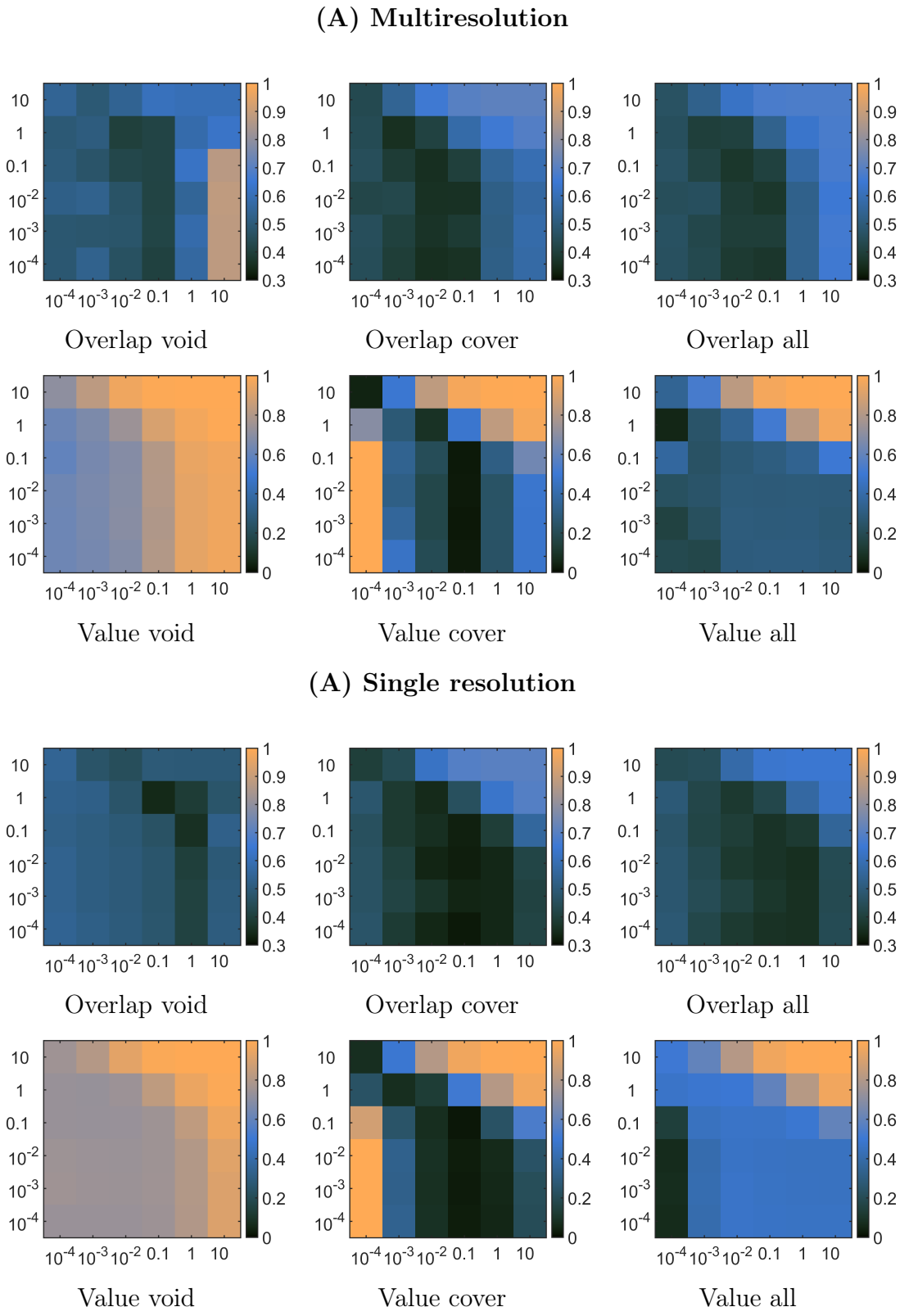

Figure 5.1 *Error of the relative overlap and error of the value with dense configuration for void, cover and whole area. In each graph the parameter α is on the x-axis and the parameter β on the y-axis.*

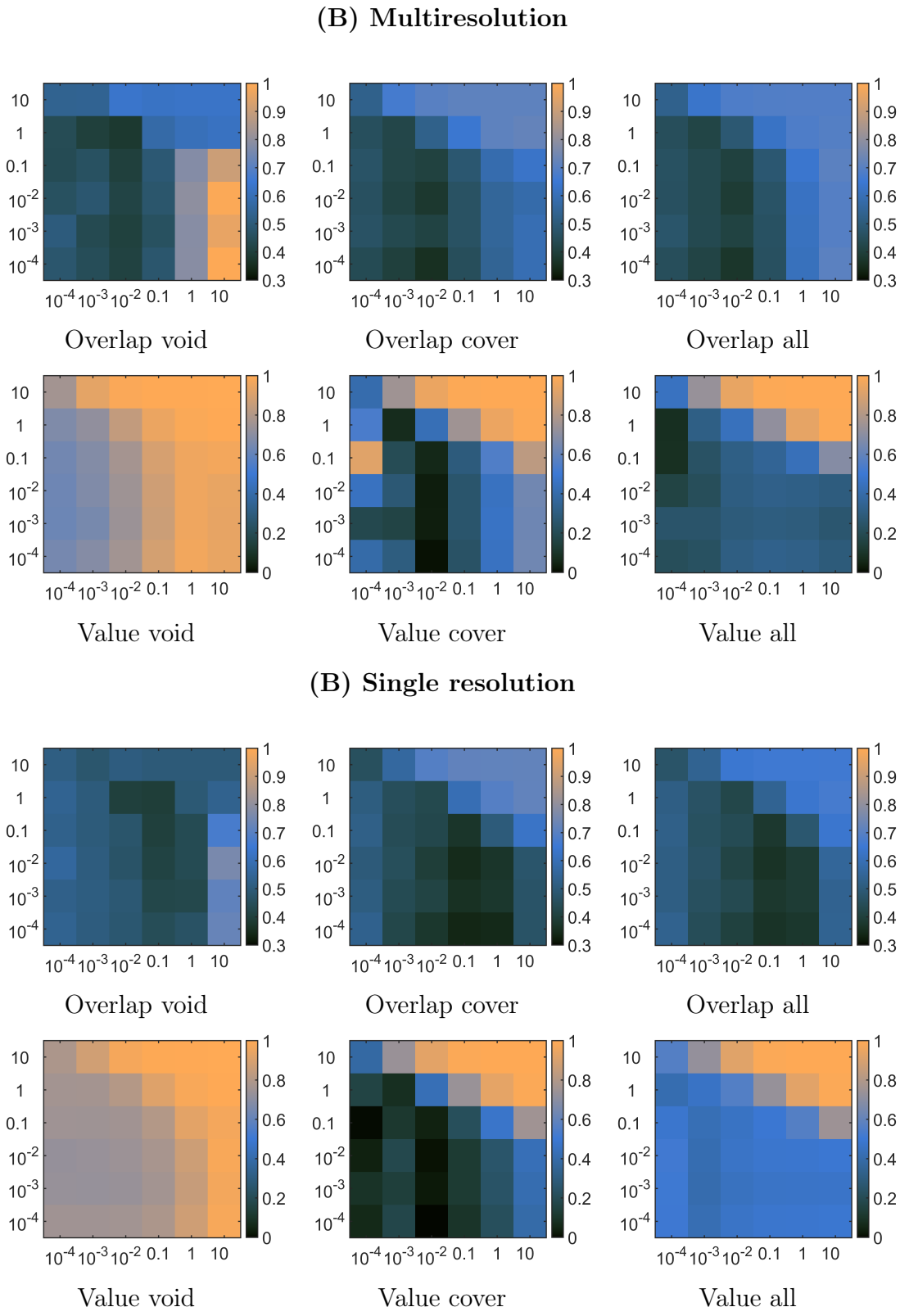

Figure 5.2 *Error of the relative overlap and error of the value with normal configuration for void, cover and whole area. In each graph the parameter α is on the x-axis and the parameter β on the y-axis.*

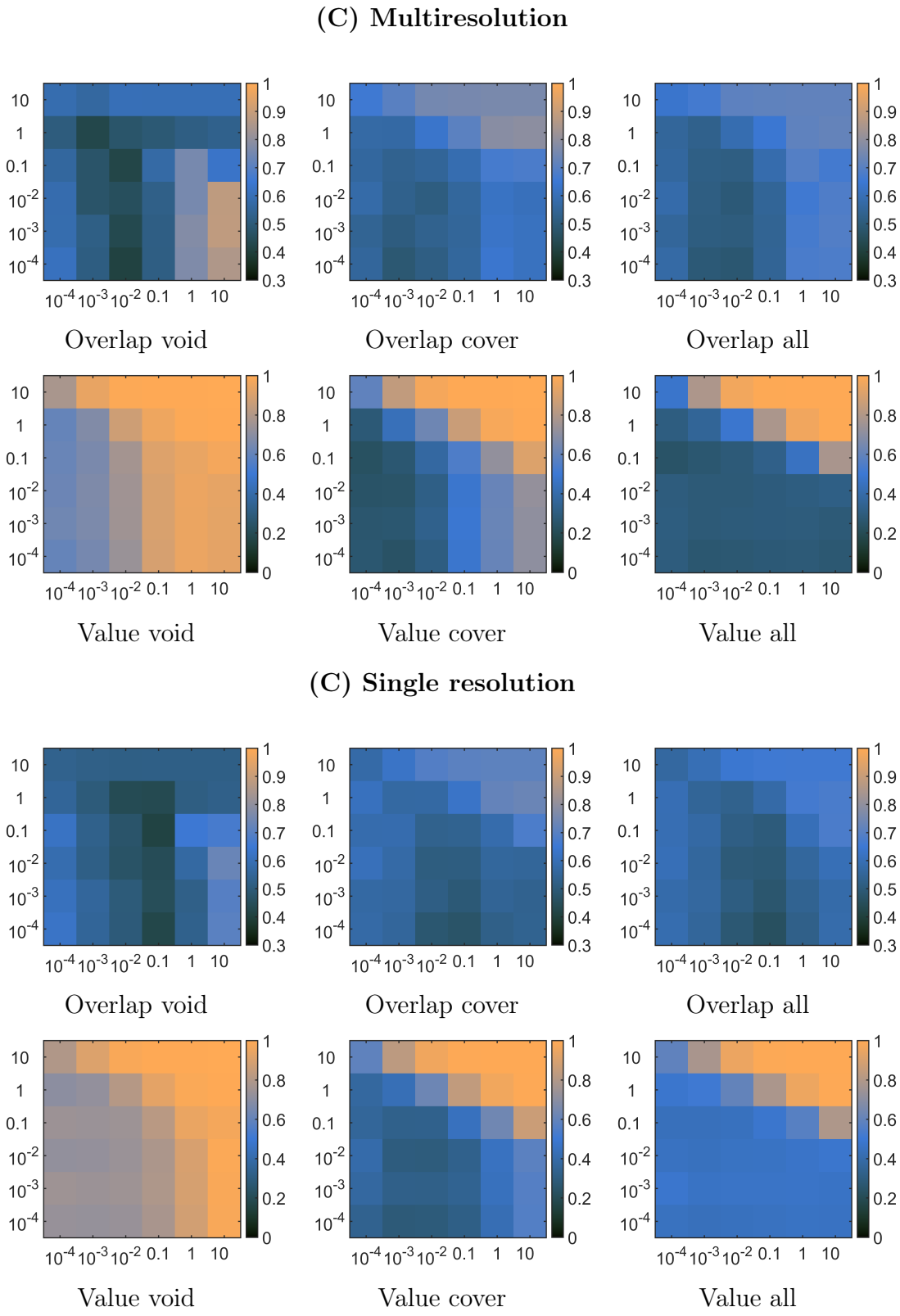

Figure 5.3 *Error of the relative overlap and error of the value with sparse configuration for void, cover and whole area. In each graph the parameter α is on the x-axis and the parameter β on the y-axis.*

5.3 Total variation

The graphs illustrating the total variatons seems to be quite the same for every configuration (A), (B) and (C) and for both single and multiresolution approach. In every case total variation tends to depend more on the parameter α than β. In every occasion the smallest values of total variations were reached with bigger values of parameter α and total variation was at its highest in every occasion when the value of α was chosen to be 10^{-4}. With bigger values of α total variation appeared to be almost zero whereas with smaller values it increased to hundreds the top values being almost 1300 with configuration (A) and single resolution.

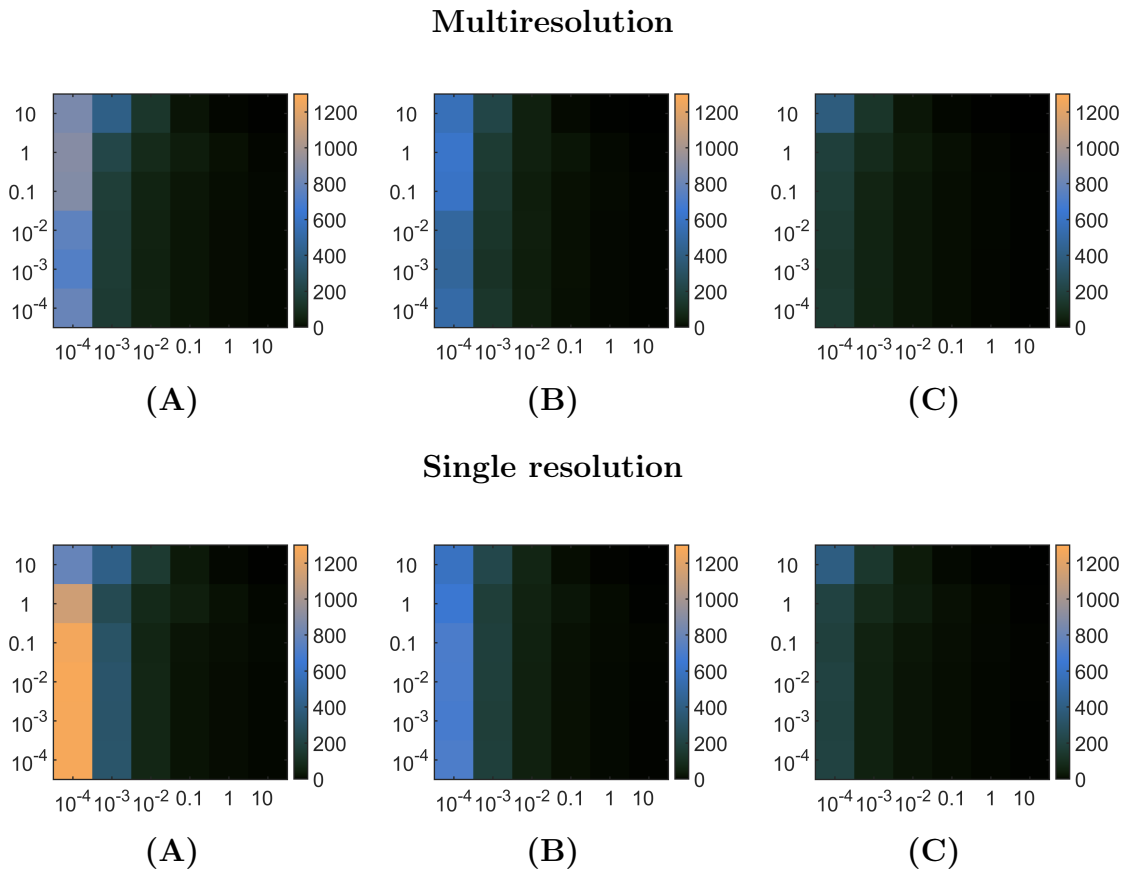

Figure 5.4 *Total variations for every three configurations (A), (B) and (C) with multi- and single resolution approaches. In each graph the parameter α is on the x-axis and the parameter β on the y-axis.*

5.4 Robustness analysis

The graphs for each of the three configurations have a strong resemblance between them. In each case the the dark grey colored curve that respresents the multiresolution seems to go above the green colored curve that represents the single resolution

when the threshold is chosen to be small enough. In each case the curves cross at some point that means that it is the point from which the single resolution starts to give better results than the multiresolution. In graph (A) the curves also cross later but it is not as significant as the first crossing point. In cases (A) and (B) the first crossing point is approximately at threshold level 45% and in case (C) at threshold level 55%. This means that with every three configurations when the parameters α and β can be selected as desired the multiresolution approach suits better in every three cases. Based on these results it also seems that the range of the parameters that are more suitable with multiresolution is bigger when the configuration is sparser.

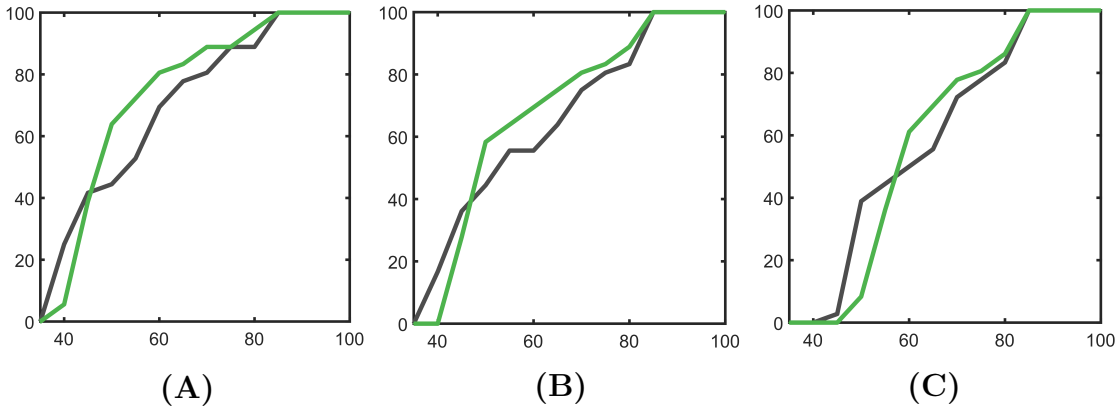

Figure 5.5 *Robustness analysis for different signal configurations. In each graph the gray line indicates multiresolution and the green line singleresolution. On the x-axis is the chosen threshold below which the values are taken into account and on the y-axis is the percentage of these values with respect to all values.*

5.5 Reconstructions

Reconstructions were here computed to get examples of both resolution approaches. The reconstructions were created for single resolution and for the three different levels of multiresolution that were the coarse, the normal and the fine resolution. Each reconstruction was formed using the value of 0.01 for both parameters α and β. That value was chosen since it appeared to give relatively good results with each configuration. These reconstructions together with the relative overlaps of these reconstructions with respect to the exact construction are illustrated in figures 5.7, 5.8 and 5.9. Picture of the exact construction that was the target of the inversion is shown in figure 5.6

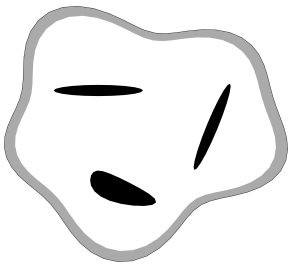

Figure 5.6 *Picture of the exact construction to be recovered. Dark inclusion model vacuum cavities and the grey part the surface layer which were the targets of the inversion.*

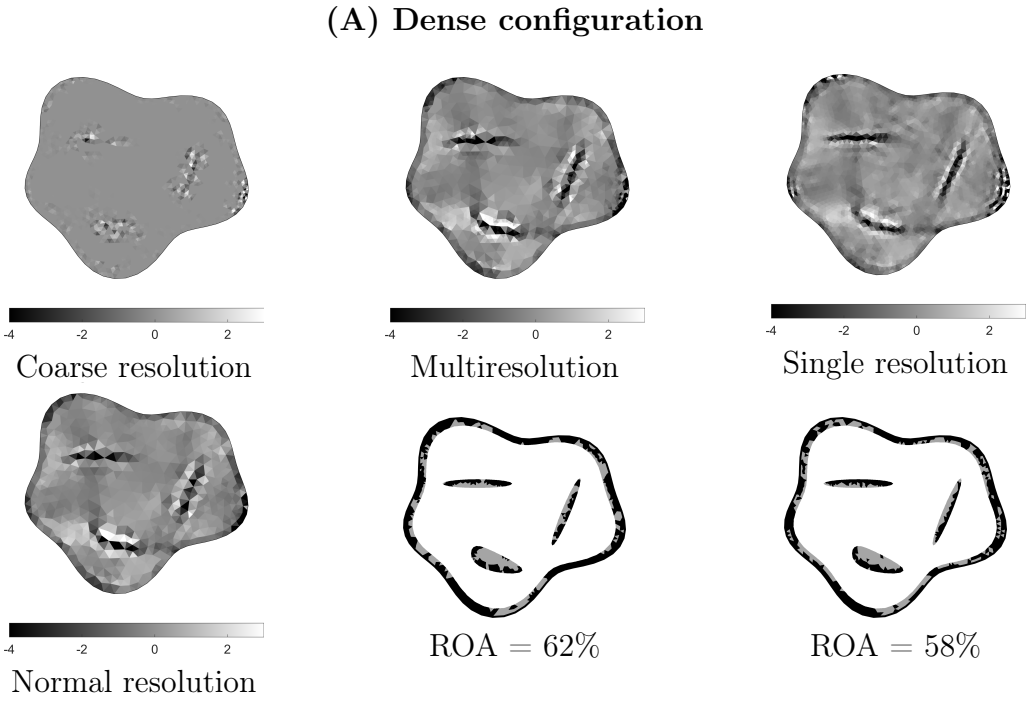

Figure 5.7 *Reconstructions and relative overlaps for signal configuration (A) with multi- and single resolution. The multiresolution reconstruction is formed as a sum of the normal and coarse resolution constructions.*

(B) Medium configuration

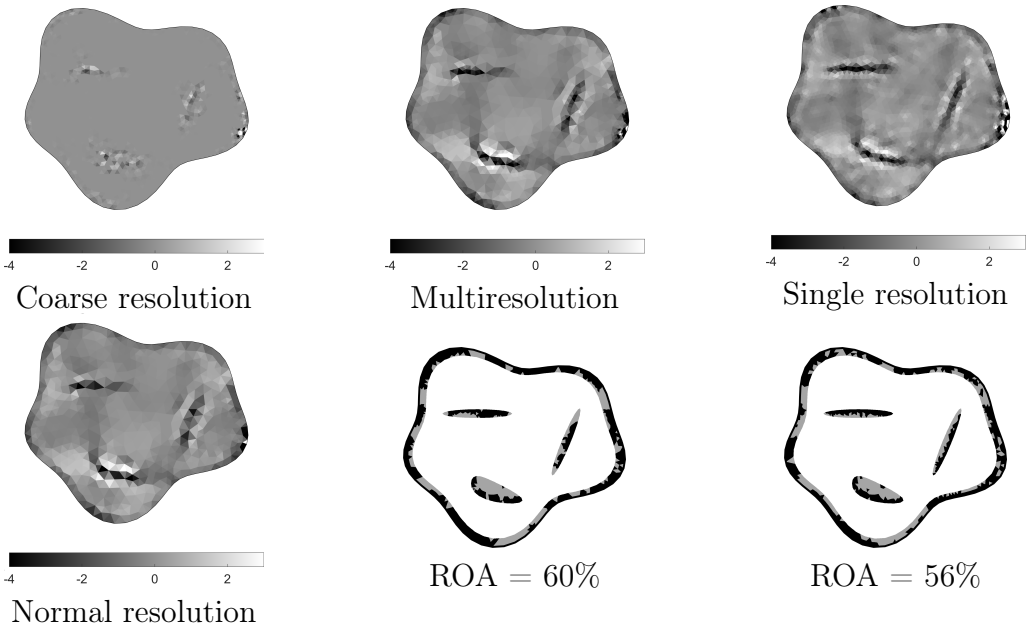

Figure 5.8 *Reconstructions and relative overlaps for signal configuration (A) with multi- and single resolution. The multiresolution reconstruction is formed as a sum of the normal and coarse resolution constructions.*

(C) Sparse configuration

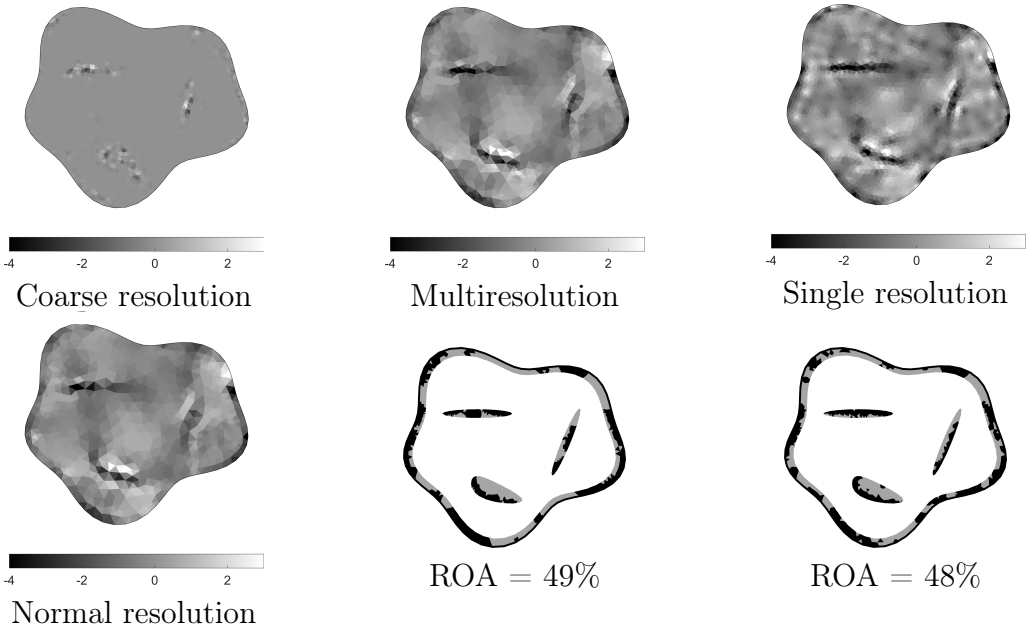

Figure 5.9 *Reconstructions and relative overlaps for signal configuration (A) with multi- and single resolution. The multiresolution reconstruction is formed as a sum of the normal and coarse resolution constructions.*

6. DISCUSSION

In this work, a multiresolution approach to waveform tomography inverse problem was introduced and tested. The results were compared to using a single resolution approach as a reference. In the numerical experiments a minimal three-source configuration was used with three different sparsity levels of the signal. The experiments concentrated on the sparsity/density of the data recording points and on the choice of the regularization parameters.

Based on the results, multiresolution turned out be a valid alternative to single resolution with all the three signal configuration. The results actually were more accurate with multiresolution when the regularization parameters were chosen optimally. The sparsity of the signal also affected the results as was expected. With the medium configuration the reconstruction quality was only slightly inferior than with the dense one. With the sparse configuration the reconstruction quality dropped significantly.

From the memory consumption viewpoint the use of medium configuration instead of the dense configuration is very advantageous. This combined with the use of multiresolution resulted in significant savings in computation of matrix $\mathbf{L}$ containing the differentiated signal data. The memory usage of $\mathbf{L}$ in our 2D model is quadratically proportional to the frequency of data recording points as well as to the frequency of the pixels in the reconstructed image.

However, in practice most of the possible real life applications require a 3D-model in order to achieve better and desired results, even though, the 2D-model may be sufficient or even more suitable with some applications. This is why the main focus in possible future experiments should be in the inspection and development of the 3D-model. With the 3D-model the memory saving approach is even more crucial as the growth of the memory usage comes cubic instead of the quadratic growth in 2D-model. For example if the number of data points is cut to the quarter (medium configuration) and the resolution of the image is cut to the half with the original frequencies being f_1 and f_2, the memory usage drops to only

$$\left(\frac{1}{2}f_2\right)^3\left(\frac{1}{2}f_1\right)^2 f_1 = \frac{1}{256}f_1^3 f_2^3. \tag{6.1}$$

In this thesis the sparsity of the data was only handled spationally, but temporal filtering could also be one of the interests in the future experiments. One possbile method to discretize the data temporally is for example a discrete cosine transform (DCT). Also different and more efficient ways of data packing should be considered.

Also, instead of using the whole signal itself, in some cases the use of different and more simple methods could be beneficial not only from the memory consumption viewpoint, but also the robustness could be better. For example, in the inspection of soil or bedrock the properties of the subsurface could be so complicated that the use of a simpler method could be advantageous. The inspected material could for instance have some polarizing properties that could alter the results significantly. In this type of case the use of a travel-time data

$$t = \frac{\int tu^2 dt}{\int u^2 dt} \tag{6.2}$$

or total energy of the signal

$$E = \int u^2 dt \tag{6.3}$$

can be profitable.

The mathematical model in this work was precisely formulated and unique as equivalent model has not been introduced before. The multiresolution technique was based on multigrid methods that enabled the use of more sparse mesh [15] [41], [42] which led to speed gains and the convergence in computations. Multiresolution could also be done using other techniques such as a wavelet-based method in which the main focus is in the packing of the propagating wave [43], [44], [45], [46], [47], [48] [49], [50], [51].

However, in the computations only computer simulated data was used, but in the future it would be interesting to test the model in practice with some real recorded data. For example, very simple experiments could be performed with a setup of basic microphones and speakers. If the results of these simple experiments turned out to be good enough, also a test with data from some real life application such as

biomedical or gephysical experiments could be feasible.

7. CONCLUSIONS

This thesis both introduced and executed a multiresolution approach to a waveform tomograhy inverse problem as an alternative to single resolution approach. Numerical experiments of this thesis concentrated in the sparsity/density of the data recording points and the choice of the regularization parameters α and β. The experiments were only performed using a 2D-model but it would be interesting to see this kind of method used for the 3D-model as well in the future experiments.

The main benefit of using the multiresolution approach instead of the single resolution one is that it enables a speedup in calculation of the process. This is because the amount of data needed in the simulation is much smaller than with single resolution.

The multiresolution approach also turned out to be more precise than the single resolution one regardless of the density of data points under suitable circumstances. This means that when the parameters could be chosen appropriately the multiresolution was proven to be the best way to solve the inversion problem. The sparsity of the data points also had a significant effect on the results. The more dense data configuration was chosen the more precise were the inversion results. However, it should be noticed that the difference between the dense and the medium configuration was relatively small compared to the memory savings.

BIBLIOGRAPHY

[1] J. P. Kaipio and E. Somersalo, *Statistical and Computational Inverse Problems.* Berlin: Springer, 2005.

[2] C. Hellier, *Handbook of Nondestructive Evaluation, Second Edition.* McGraw-Hill Professional, 2012. [Online]. Available: http://mhebooklibrary.com/doi/book/10.1036/9780071777131

[3] J. Brittan, J. Bai, H. Delome, C. Wang, and D. Yingst, "Full waveform inversion - the state of the art," *First Break*, vol. 31, no. 10, October 2013.

[4] N. V. e. a. Ruiter, "3d ultrasound computer tomography of the breast: A new era?" *European Journal of Radiology*, vol. 81, pp. 133–134, 2012.

[5] J. E. Joy, E. E. Penhoet, and D. B. Petitti, *Saving Women's Lives: Strategies for Improving Breast Cancer Detection and Diagnosis.*

[6] S. Semenov, "Microwave tomography: review of the progress towards clinical applications," *Philosophical Transactions of the Royal Society of London A: Mathematical, Physical and Engineering Sciences*, vol. 367, no. 1900, pp. 3021–3042, 2009.

[7] J. Greenleaf and R. Bahn, "Clinical imaging with transmissive ultrasonic computerized tomography," *Biomedical Engineering, IEEE Transactions on*, vol. BME-28, no. 2, pp. 177–185, Feb 1981.

[8] A. C. Kak and M. Slaney, *Principles of Computerized Tomographic Imaging.* IEEE Press, 1988.

[9] A. Lorenzi, F. T. Tisbierek, and L. C. P. da Silva Filho, "Ultrasonic pulse velocity analysis in concrete specimens." Buenos Aires: In the proceedings of IV Conferencia Panamericana de END, October 2007.

[10] *PUNDIT*, Germann Instruments, available: http://www.germann.org/TestSystems/PUNDIT/PUNDIT.pdf.

[11] D. J. Daniels, *Ground Penetrating Radar*, 2nd ed. Institution of Engineering and Technology, 2004.

[12] W. Munk and C. Wunsch, "Observing the Ocean in the 1990s," *Philosophical Transactions of the Royal Society of London Series A*, vol. 307, pp. 439–464, Oct. 1982.

[13] W. Munk, P. Worcester, and C. Wunsch, *Ocean Acoustic Tomography.* Cambridge University Press, 1995.

[14] J. B. Schneider, *Understanding the Finite-Difference Time-Domain Method.* John B. Schneider, 2012, Available: http://www.eecs.wsu.edu/~schneidj/ufdtd/ufdtd.pdf.

[15] D. Braess, *Finite Elements: Theory, Fast Solvers and applications in Solid Mechanics.* Cambridge University Press, 2006.

[16] L. Y. H., *Introduction to Engineering Electromagnetics.* Springer, USA, 2013.

[17] S. J. Orfanidis, *Electromagnetic Waves and Antennas.* ECE Department Rutgers University, 2008.

[18] H. Koskinen and A. Viljanen, "Elektrodynamiikka," 2008, available: http://space.fmi.fi/~viljanea/ed2008/ED2007_09.pdf.

[19] "Advanced electromagnetism part 2: Electromagnetic waves in dielectric media," available: http://pcwww.liv.ac.uk/~awolski/Teaching/Liverpool/PHYS370/AdvancedElectromagnetism-Part2.pdf.

[20] C. Cronström and P. Lipas, *Johdatus sähködynamiikkaan ja suhteellisuusteoriaan.* Limes, 2000.

[21] "Advanced electromagnetism part 3: Electromagnetic waves in conducting media," available: http://pcwww.liv.ac.uk/~awolski/Teaching/Liverpool/PHYS370/AdvancedElectromagnetism-Part3.pdf.

[22] W. T. B. Kelvin, *Baltimore lectures on molecular dynamics and the wave theory of light.* London : C. J. Clay and Sons ; Baltimore : Publication Agency of the Johns Hopkins University, 1904.

[23] R. P. Feynman, R. B. Leighton, and M. L. Sands, *The Feynman Lectures on Physics.* Addison-Wesley, 1969, vol. 1.

[24] T. Grzegorczyk, P. Meaney, P. Kaufman, R. di Florio-Alexander, and K. Paulsen, "Fast 3-d tomographic microwave imaging for breast cancer detection," *Medical Imaging, IEEE Transactions on*, vol. 31, no. 8, pp. 1584–1592, Aug 2012.

[25] W. Munk, "Ocean acoustic tomography," in *Physical Oceanography*, M. Jochum and R. Murtugudde, Eds. Springer New York, 2006, pp. 119–138. [Online]. Available: http://dx.doi.org/10.1007/0-387-33152-2_8

[26] L. Evans, *Partial Differential Equations*, ser. Graduate studies in mathematics. American Mathematical Society, 1998.

[27] A. Bossavit and L. Kettunen, "Yee-like schemes on a tetrahedral mesh, with diagonal lumping," *International Journal of Numerical Modelling: Electronic Networks, Devices and Fields*, vol. 12, no. 1–2, pp. 129–142, 2009.

[28] K. Yee, "Numerical solution of initial boundary value problems involving maxwell's equations in isotropic media," *IEEE Transactions on Antennas and Propagation*, vol. 14, no. 3, pp. 302–307, 1966.

[29] C. Altman and K. Suchy, *Reciprocity, Spatial Mapping and Time Reversal in Electromagnetics*, ser. Developments in Electromagnetic Theory and Applications.

[30] O. Scherzer, M. Grasmair, H. Grossauer, and F. L. M. Haltmeier, *Variational Methods in Imaging*, ser. Applied Mathematical Sciences. Springer New York, 2008.

[31] W. Stefan, *Total Variation Regularization for linear Ill-posed Inverse Problems: Extensions and Applications.* Arizona State University, 2008.

[32] S. Pursiainen and M. Kaasalainen, "Detection of anomalies in radio tomography of asteroids: Source count and forward errors," *Planetary and Space Science*, vol. 99, pp. 36 – 47, September 2014.

[33] ——, "Sparse source travel-time tomography of a laboratory target: accuracy and robustness of anomaly detection," *Inverse Problems*, vol. 30, no. 11, p. 114016, 2014. [Online]. Available: http://stacks.iop.org/0266-5611/30/i=11/a=114016

[34] W. Bottke, *Asteroids III*, ser. University of Arizona space science series. University of Arizona Press, 2002.

[35] A. Herique, J. Gilchrist, W. Kofman, and J. Klinger, "Dielectric properties of comet analog refractory materials," *Planetary and Space Science*, vol. 50, no. 9, pp. 857 – 863, 2002, space Related Laboratory Investigation: Materials, environments a nd life. [Online]. Available: http://www.sciencedirect.com/science/article/pii/S0032063302000600

[36] J. L. Davis and A. P. Annan, "Ground-penetrating radar for high-resolution mapping of soil and rock stratigraphy," *Geophysical Prospecting*, vol. 37, no. 5, pp. 531–551, 1989. [Online]. Available: http://dx.doi.org/10.1111/j.1365-2478.1989.tb02221.x

[37] J. Irving and R. Knight, "Numerical modeling of ground-penetrating radar in 2-d using matlab," *Computers & Geosciences*, vol. 32, no. 9, pp. 1247 – 1258, 2006. [Online]. Available: http://www.sciencedirect.com/science/article/pii/S0098300405002621

[38] F. J. Harris, "On the use of windows for harmonic analysis with the discrete fourier transform," *Proceedings of the IEEE*, vol. 66, no. 1, pp. 51–83, Jan 1978.

[39] A. Nuttall, "Some windows with very good sidelobe behavior," *IEEE Transactions on Acoustics, Speech, and Signal Processing*, vol. 29, no. 1, pp. 84–91, Feb 1981.

[40] D. Colton and R. Kress, *Inverse Acoustic and Electromagnetic Scattering Theory, Second Edition*, 1998.

[41] S. Oh, C. A. Bouman, and K. J. Webb, "Multigrid tomographic inversion with variable resolution data and image spaces," *Image Processing, IEEE Transactions on*, vol. 15, no. 9, pp. 2805–2819, 2006. [Online]. Available: http://dx.doi.org/10.1109/tip.2006.877313

[42] S. Oh, A. B. Milstein, C. A. Bouman, and K. J. Webb, "Multigrid algorithms for optimization and inverse problems," in *Computational Imaging*, ser. SPIE, C. A. Bouman and R. L. Stevenson, Eds., vol. 5016, Jun. 2003, pp. 59–70.

[43] A. H. Delaney and Y. Bresler, "Multiresolution tomographic reconstruction using wavelets," in *Image Processing, 1994. Proceedings. ICIP-94., IEEE International Conference*, vol. 2, Nov 1994, pp. 830–834 vol.2.

[44] N. Lee, "Wavelet-vaguelette decompositions and homogeneous equations," p. 93, 1997, copyright - Database copyright ProQuest LLC; ProQuest does not claim copyright in the individual underlying works; Last updated - 2016-03-14. [Online]. Available: http://search.proquest.com/docview/304374032?accountid=27303

[45] B. Sahiner and A. E. Yagle, "Image reconstruction from projections under wavelet constraints," *IEEE Transactions on Signal Processing*, vol. 41, no. 12, pp. 3579–3584, Dec 1993.

[46] M. Bhatia, W. C. Karl, and A. S. Willsky, "A wavelet-based method for multiscale tomographic reconstruction," *Medical Imaging, IEEE Transactions on*, vol. 15, no. 1, pp. 92–101, 1996. [Online]. Available: http://dx.doi.org/10.1109/42.481444

[47] ——, "Tomographic reconstruction and estimation based on multiscale natural-pixel bases," *IEEE Transactions on Image Processing*, vol. 6, no. 3, pp. 463–478, Mar 1997.

[48] R. Scapaticci, I. Catapano, and L. Crocco, "Wavelet-based adaptive multiresolution inversion for quantitative microwave imaging of breast tissues," *IEEE Transactions on Antennas and Propagation*, vol. 60, no. 8, pp. 3717–3726, Aug 2012.

[49] I. Daubechies, *Ten Lectures on Wavelets*. Philadelphia, PA, USA: Society for Industrial and Applied Mathematics, 1992.

[50] S. G. Mallat, "A theory for multiresolution signal decomposition: the wavelet representation," *IEEE Transactions on Pattern Analysis and Machine Intelligence*, vol. 11, no. 7, pp. 674–693, Jul 1989.

[51] B. Jawerth and W. Sweldens, "An overview of wavelet based multiresolution analyses," *SIAM Review*, vol. 36, no. 3, pp. 377–412, 1994. [Online]. Available: http://www.jstor.org/stable/2133070